Epidermal Collagen Reduction Drives Selective Aspects of Aging in Sensory Neurons

Meera M. Krishna[1,2], Swapnil G. Waghmare[1,2], Ariel L. Franitza[2], Emily C. Maccoux[2], Lezi E[1,2,*]

[1]Department of Cell Biology, Neurobiology and Anatomy, Medical College of Wisconsin, 8701 W Watertown Plank Road, Milwaukee, WI 53226, United States of America

[2]Neuroscience Research Center, Medical College of Wisconsin, 8701 W Watertown Plank Road, Milwaukee, WI 53226, United States of America

[*]Corresponding author/Lead contact:
lezie@mcw.edu
+1-414-955-2248

Running Title: Epidermal Collagen Reduction Drives Neuronal Aging

ABSTRACT

Despite advances in understanding molecular and cellular changes in the aging nervous system, the upstream drivers of these changes remain poorly defined. Here, we investigate the roles of non-neural tissues in neuronal aging, using the cutaneous PVD polymodal sensory neuron in *Caenorhabditis elegans* as a model. We demonstrate that during normal aging, PVD neurons progressively develop excessive dendritic branching, functionally correlated with age-related proprioceptive deficits. Our study reveals that decreased collagen expression, a common age-related phenomenon across species, triggers this process. Specifically, loss-of-function in *dpy-5* or *col-120*, genes encoding cuticular collagens secreted to the epidermal apical surface, induces early-onset excessive dendritic branching and proprioceptive deficits. Adulthood-specific overexpression of *dpy-5* or *col-120* mitigates excessive branching in aged animals without extending lifespan, highlighting the specific role of these collagens in promoting neuronal healthspan. Notably, collagen reduction specifically drives excessive branching in select sensory neuron subclasses but does not contribute to dendritic beading, another aging-associated neurodegenerative phenotype distinctively associated with a different mechanosensitive dysfunction. Lastly, we identify that *rig-3*, an Immunoglobulin Superfamily member expressed in interneurons, acts upstream of collagen genes to maintain PVD dendritic homeostasis during aging, with downstream requirement of *daf-16*/FOXO. These findings reveal that age-related collagen reduction cues neuronal aging independently of collagen's traditional structural support function, potentially involving bi-directional communication processes between neurons and non-neuronal cells. Our study also offers new insights into understanding selective neuron vulnerability in aging, emphasizing the importance of multi-tissue strategies to address the complexities of neuronal aging.

Key Words: Aging; neuronal aging; sensory neurons; collagen; epidermis; *Caenorhabditis elegans*

1. INTRODUCTION

Age represents a significant risk factor for many neurological disorders, including peripheral neuropathies. While several factors such as diabetes, autoimmune diseases, physical injury, and vitamin imbalances contribute to neuropathies, aging not only increases susceptibility to these conditions but also raises the prevalence of idiopathic neuropathies (Hicks et al., 2021). Currently, our limited ability to treat neuropathies in elderly populations largely stems from gaps in understanding the mechanisms driving the aging of the nervous system. Signaling from non-neural tissues may be a promising avenue to address this gap.

Non-neural tissues, such as the skin, play essential roles in the development of the peripheral nervous system. Studies show that neurotrophic factors in the skin guide sensory innervation, with overexpression of neurotrophin-4 in mouse epidermal basal cells leading to excessive sensory endings in the dermal footpad (Krimm et al., 2006). Similarly in *C. elegans*, the morphogenesis of the PVD neuron, a cutaneous sensory neuron with an elaborate dendritic arbor, relies on SAX-7, an epidermally-expressed cell-adhesion molecule, along with other extracellular proteins, that precisely guide dendritic arborization (Dong et al., 2013; Salzberg et al., 2013). Epidermal ensheathment is a process where epidermal cells wrap around growing neurites of sensory neurons to regulate branching morphogenesis, which is also highly dependent on two-way signaling between the neuron and the skin; blocking sheath formation in *Drosophila* and zebrafish destabilizes dendrite branches and reduces nociceptive function (Jiang et al., 2019). However, whether non-neural tissues also actively contribute to the aging of the peripheral nervous system remains less understood.

As neurons age, they undergo structural deterioration, leading to synapse loss and impaired, signal transmission, and ultimately behavioral abnormalities. Neuritic beading, also known as focal swelling or blebbing, is an evolutionarily conserved aging-associated structural change indicative of neurodegeneration (Takeuchi et al., 2005). These neuritic beads, often consisting of broken-down cytoskeletal and motor protein components, disrupt organelle transport, such as mitochondrial trafficking, leading to bioenergetic dysfunction and eventual neuronal death (Takeuchi et al., 2005). Our previous research in *C. elegans* has shown that age-related upregulation of antimicrobial peptides (AMPs) in the skin triggers dendritic beading in PVD

neurons, accompanied by mechanosensory decline, demonstrating a significant role for skin-derived molecular cues in sensory neuron aging (E et al., 2018).

Increased aberrant neurite branching is another age-related structural change, documented in the peripheral nervous systems of elderly human patients with sensory neuropathies (Lauria et al., 1999). While it has been speculated that the increased branching may compensate for other aging-associated structural and functional losses, this counterintuitive phenomenon is not well understood. Interestingly, *C. elegans* PVD neurons also exhibit a pronounced increase in dendritic branching in advanced age, as noted in our prior work (E et al., 2018) and in a separate study by Kravtsov et al. (Kravtsov et al., 2017), though the functional implications and precise underlying mechanisms remain unknown. It is noteworthy that the aging-associated excessive branching, unlike the dendritic beading, does not appear to be regulated by skin AMPs, suggesting the involvement of alternative mechanisms.

In this study, we provide an in-depth characterization of aging-associated excessive dendritic branching in PVD neurons, demonstrating its functional relevance to age-related decline in proprioception. Using PVD neuron as a model, we further discover that mutations or downregulation of two cuticular collagen genes, *dpy-5* and *col-120*, induce early-onset excessive dendritic branching and proprioceptive deficits, suggesting that age-dependent reduction of skin collagens plays a causative role in sensory neuron aging. Moreover, overexpression of these collagen genes mitigates the severity of excessive branching in aged animals. Importantly, our results also indicate that the regulatory role of skin collagens is specific to branching integrity during aging and is limited to certain types of cutaneous sensory neurons. Additionally, we identify RIG-3, a neuronal Immunoglobulin Superfamily protein, as an upstream partner in skin collagen's regulation of PVD dendritic integrity, with downstream involvement of DAF-16/FOXO. These findings reveal a novel role for collagens in actively regulating sensory neuron aging, expanding our understanding of the upstream molecular mechanisms that drive nervous system aging.

2. RESULTS

2.1 Aging triggers progressive development of excessive higher-order dendritic branching in PVD sensory neurons

To investigate how skin tissues impact sensory neuron aging, we used the PVD neuron in *C. elegans* as a model. PVD is a cutaneous mechanosensory neuron, involved in harsh touch, cold sensation, and proprioception, extending dendrites across the body (Chatzigeorgiou et al., 2010; Tao et al., 2019). Each animal possesses two PVD neurons, PVDR on the right and PVDL on the left, with dendritic branches extending dorsally and ventrally. Each PVD has a single axon that synapses ventrally with AVA and PVC interneurons (Figure 1a) (Smith et al., 2010; White et al., 1986). From the PVD soma, two primary (1º) dendritic branches extend anteriorly and posteriorly. Secondary (2º) dendrites emerge orthogonally from 1º branches at regular intervals, forming non-overlapping 'menorah-like' repeating units mainly composed of tertiary (3º) and quaternary (4º) dendrites (Figure 1b) (Smith et al., 2010). Our previous studies have shown that aging in PVD neurons often involves the progressive development of bead-like structures along the dendrites (Figure S1a) (E et al., 2018), resembling morphological changes observed in human patients with peripheral neuropathies (Faerman et al., 1982). Majority of the beading structures in PVD dendrites indicate a disrupted microtubule network and are associated with age-related deficits in the harsh touch sensing function of PVD neurons (Figure S1b) (E et al., 2018).

In this study, we focused on and conducted a thorough characterization of another distinctive aging phenotype of PVD neurons – excessive dendritic branching, previously noted in literature (E et al., 2018; Kravtsov et al., 2017) yet lacking clarification regarding its functional implications and underlying mechanisms. Our analysis revealed a progressive and substantial increase in the number of 5º and 6º dendritic branches from Day 1 (D1) to D9 of adulthood in control (CT) animals (Figure 1c-e, Figure S1c-f), while the number of 4° dendrites or PVD menorahs remained mostly unchanged (Table S1). This phenotype was observed consistently regardless of FUDR use for synchronizing age (see Methods) (Table S1). Notably, no age-related ectopic branching was detected in the axons. To confirm that this branching is an inherent consequence of aging, we first utilized the environment temperature-lifespan correlation in *C. elegans*, where higher temperatures accelerate aging, while lower temperatures decelerate it (Klass, 1977). Our findings revealed a temperature-dependent variation in the severity and progression of PVD dendritic branching (Figure 1f-g). We further assessed branching in lifespan-affecting mutants, focusing on DAF-2/insulin-like signaling and mitochondrial pathway, given their well-established roles in aging (Ishii et al., 1998; Lee & Lee,

2022). In short-lived *daf-16(mu86)* mutants, excessive branching appeared earlier and progressed rapidly with age; *mev-1(kn1)* mutants with similarly short lifespans showed the same trend (Figure 1h, Figure S1g-i). Notably, long-lived *daf-2(e1370)* mutants displayed excessive branching similar to CT animals at D9, consistent with previous findings by Kravtsov et al. (Figure S1j).

Additionally, the increase in higher-order (≥ 5°) dendritic branching persisted after accounting for the slight age-related increase in body length (Figure S1m-n), indicating it is not merely growth-related. The extent and progression of branching were comparable between PVDL and PVDR throughout aging (Table S1). While slight variations were noted between the dorsal and ventral sides, the overall increase in branching remained consistent on both sides (Table S1). This pattern held even after normalizing for the number of PVD 'menorah' structures or 4° branches (Figure 1i-l, Table S1). Using the PVD soma position as a reference point, a similar increase was observed in both anterior and posterior sections (Figure 1m-p, Table S1), Together, these data suggest that excessive branching in PVD higher-order dendrites is an intrinsic feature of aging.

2.2 Cytoskeletal composition of higher-order branches in aging PVD neurons

During development, stabilized microtubules are often found in large primary dendrites, while actin is abundant in small higher-order dendrites or dendritic spines, supporting anatomical plasticity (Kaech et al., 2001). To examine the cytoskeletal composition of the aging-associated higher-order dendritic branches in PVD neurons, we used transgenic strains expressing *ser-2(3)p::EMTB::GFP* and *ser-2(3)p::GFP::UtrCH* to visualize polymerized microtubules and actin filaments, respectively, in PVD neurons (E et al., 2018). We found that microtubules were absent in >3° branches in both aged and young adult CT animals (Figure S2a). Time-lapse imaging analysis of young adult CTs revealed abundant F-actin in 4° dendrites and at the leading edges of occasional higher-order branches, with the excessive 5°/6° branches in aged CTs primarily consisting of F-actin as well (Figure 1q, Figure S2b). Further quantitative analysis indicated dynamic remodeling of F-actin-rich higher-order branches in both young and aged CTs, with frequent outgrowths and retractions (Figure 1r-s). Notably, during the same observation period, ≥ 5° branches in aged animals tended to gain length, while those in young

adults appeared more tightly regulated from further growth (Figure 1t). This regulation is likely independent of pruning or phagocytosis, as no fluorescent neuronal debris was observed near remodeled regions. These findings suggest that a localized mechanism restricting dendritic growth may be lost with aging.

2.3 Aging-associated excessive dendritic branching in PVD neurons correlates with proprioceptive deficits

To explore the functional implications of the excessive branching in aging PVD neurons, we first examine its relevance to noxious harsh touch sensation, a process relying on proper PVD synaptic connections with downstream command interneurons for initiating escape movements (Chatzigeorgiou et al., 2010; E et al., 2018). To correlate neuronal morphological changes with functional outcomes, we performed harsh touch assays with individual animals and subsequently analyzed PVD branching in the same animals. Interestingly, age-related decline in harsh touch response in CTs (E et al., 2018) showed no correlation with excessive branching (Figure S3a).

As a polymodal neuron, PVD senses multiple stimuli. The integrity of its dendritic menorah structures is essential for the sensory aspect of proprioceptive regulation, independent of its axon's synaptic function (Tao et al., 2019). Proprioception, the processing of sensorimotor input for posture control and movement, can be assessed in *C. elegans* by measuring track patterns left by the worms on bacterial lawns (Figure 2a). Mutations in *dma-1* or related genes disrupting PVD menorah structures (characterized by absence of ≥ 2° branches) reduce track wavelength and amplitude (Tao et al., 2019). We therefore hypothesized that excessive branching in aging PVD neurons could manifest as proprioceptive deficits.

Our data showed that both the mean amplitude and mean wavelength of sinusoidal movements were significantly reduced in aged CT animals, compared to young (Figure 2b-c). Additionally, aged CT animals displayed increased intra-individual variability in both amplitude and wavelength (Figure 2d-e). These age-related changes resemble the gait pattern changes observed in elderly humans, such as decreased stride length/step width and greater variability, which are strongly linked to a decline in proprioception (Callisaya et al., 2010; Wiesmeier et al., 2015). A within-individual correlation analysis further showed that the extent of 'higher-order'

branches, particularly dorsal branches, was negatively correlated with mean amplitude and wavelength, while the severity of excessive branching, regardless of orientation, positively correlated with variability in track amplitude and wavelength (Figure. 2f-i, Table S2). These findings reveal a novel link between aging-associated excessive branching of PVD dendrites and proprioceptive deficits in aging.

Interestingly, there appears to be an absence of concurrence of PVD dendritic beading and excessive branching within individual animals; rather, a negative correlation seems evident, with animals showing pronounced beading less likely to exhibit severe branching, and vice versa (Figure S3b-c). Combined with the distinct behavioral manifestations of beading and excessive branching (E et al., 2018) (Figure 2, Figure S1b, Figure S3a), these observations suggest that aging neurons undergo a variety of morphological changes, each linked to specific functional outcomes, potentially as a compensatory mechanism to preserve certain functions especially in polymodal neurons.

2.4 Loss-of-function mutations in epidermal collagen genes induce early-onset excessive PVD dendritic branching and proprioceptive deficits

We next investigated the molecular mechanisms underlying aging-associated excessive branching. Previously, we found that aging-associated upregulation of a skin AMP contributes to PVD dendritic beading during aging, indicating that age-related skin changes can influence PVD neuron aging (E et al., 2018). However, AMP upregulation does not account for the excessive branching phenotype (E et al., 2018), prompting us to explore whether other molecular changes in the aging skin might contribute. A prime candidate is age-related decline in skin collagen gene expression, a phenomenon well-documented across species, including humans. Among the downregulated collagen genes in aging *C. elegans* (Figure S4a, GSE176088) (Teuscher et al., 2024), we examined several, including *col-120*, *col-129*, *col-141*, *dpy-5*, *dpy-10* and *rol-6*, previously studied for roles in morphogenesis and other contexts. We found that disruption of *col-120*, *col-141*, *dpy-5* and *dpy-10* via RNA interference (RNAi) or mutation resulted in early-onset excessive branching in PVD dendrites by D3, while the others had no effects (Figure 3a-i; Figure S4b-i), suggesting specific skin collagens may play a role in neuronal aging. In this study, we focused on *col-120* and *dpy-5*, as neither impacts skin

integrity or AMP gene expression, unlike *col-141* and *dpy-10* (Sandhu et al., 2021; Zhu et al., 2023), which could confound PVD aging analysis (E et al., 2018). Furthermore, the expression of *dpy-5* and *col-120* are not temporally clustered, and their proteins localize to distinct areas within the epidermal apical surface (Teuscher et al., 2024; Thacker et al., 2006), suggesting that they likely do not interact with each other functionally.

In *C. elegans*, the skin is primarily composed of a simple epithelium that secretes a collagenous cuticle to the apical side as a surface coat, creating an additional protective barrier (Chisholm & Hsiao, 2012). DPY-5 and COL-120 are classified as cuticular collagens (Teuscher et al., 2019; Thacker et al., 2006), with a domain structure similar to mammalian membrane-associated or fibril-associated collagens with interrupted triple-helices, distinguishing them from basement membrane collagens (Figure 3a). Importantly, DPY-5 and COL-120 protein levels both decrease with age in wild-type animals (Teuscher et al., 2024; Thacker et al., 2006). Although mutations in either *dpy-5* or *col-120* do not affect skin integrity (Sandhu et al., 2021; Van de Walle et al., 2019), these mutants have reduced lifespans and altered body sizes, with *dpy-5(e907)* being shorter and wider and *col-120(sy1526)* slightly elongated (Figure S4k-m). To account for body size differences, we normalized PVD dendritic branching to individual body length, confirming that early-onset excessive branching persisted in both *col-120(sy1526)* and *dpy-5(e907)* at D3 (Figure S1k-n).

We further performed rescue experiments by expressing wild-type *dpy-5* or *col-120* cDNA under their respective endogenous promoters or an epidermis-specific promoter. Both approaches successfully rescued the excessive branching phenotype in each mutant (Figure 3d-g, additional rescue lines in Figure S5). PVD neurons complete dendritic arborization around the late L4 stage (last/4th larval stage) (Smith et al., 2010). At L4, *dpy-5* and *col-120* mutants showed a slight increase in dendritic branching compared to CT animals, though not reaching the extent observed at D3 (Figure S5i-j). To confirm that excessive branching in *dpy-5* or *col-120* mutants is genuinely aging-associated, we performed adulthood-specific systemic RNAi knockdowns of these genes, initiating at late L4 and phenotyping PVD dendrites 3 days into adulthood (D3). With over 180 cuticular collagen genes in *C. elegans* (Wormbase), multiple predicted paralogs exist for both *col-120* and *dpy-5*. To ensure specificity, our RNAi clones targeted unique coding regions without homologous sequences in other collagen genes

(see Methods). RNAi effectiveness was validated by RT-qPCR (Figure S4j). CT animals fed on HT115(DE3) bacteria with empty vector L4440 (EV) exhibited aging-associated excessive branching in PVD similar to those fed on OP50 (Figure S5k-l). Our adulthood-specific RNAi approach was sufficient to induce excessive higher-order branches by D3 (Figure 3h-i, Figure S5).

Importantly, we found that D3 *col-120(sy1526)* mutants exhibited a significant decrease in both mean wavelength and amplitude of sinusoidal movement, closely resembling CT animals at D9, though without increased variability in these parameters (Figure 3j-l, Figure S5t-u). Collectively, these findings demonstrate that epidermal collagens, DPY-5 and COL-120, play a critical role in maintaining PVD dendritic branching integrity and PVD-navigated proprioceptive function during aging.

2.5 Adulthood-specific overexpression of epidermal collagen genes delays onset of excessive PVD dendritic branching

Using the *col-19* promoter (Thein et al., 2003) we overexpressed *col-120* or *dpy-5* in the epidermis, specifically during adulthood, and found that it mitigated excessive branching in PVD when examined at D9 (Figure 4a-b, Figure S6a-d). Moreover, *dpy-5* overexpression appeared to shift proprioceptive function parameters in D9 animals towards those of younger animals, though this effect did not reach statistical significance (Figure S6f-i). It is important to note that age-related declines in other systems, such as muscles and motor neurons, may complicate assessing sensory aspect of proprioception at this stage of life. Interestingly, neither *dpy-5* nor *col-120* overexpression extended lifespan (Figure 4c-d, Figure S6e). Previous studies reported a slight lifespan extension with *col-120* overexpression (Ewald et al., 2015; Goyala & Ewald, 2023; Teuscher et al., 2024); however, this discrepancy may stem from differences in promoters and 3’UTR sequences used to construct transgenic strains. Nevertheless, our findings suggest that the effects of epidermal collagen overexpression on aging primarily target neuronal health, rather than through promoting longevity.

2.6 DPY-5 and COL-120 are not involved in aging-associated PVD dendritic beading

To investigate whether skin collagen genes regulate the overall aging of PVD neurons, we examined the effects of *dpy-5* or *col*-120 mutation on the previously documented aging-associated dendritic beading phenotype (Figure S1a) (E et al., 2018). Notably, the extent of PVD dendritic beading in Day 3 *dpy-5(e907)* or *col-120(sy1526)* mutant animals was comparable to that observed in age-matched CT (Figure 5a). Coupled with our observations of a potential inverse relationship between aging-associated dendritic beading and excessive dendritic branching in older CT animals (Figure S3b-c), these results suggest that *dpy-5* and *col-120* regulate PVD dendritic structure via mechanisms separate from those leading to the dendritic beading degenerative phenotype, such as the skin AMP NLP-29 (E et al., 2018). This is also supported by previous research showing that mutations in *dpy-5* and *col-120* do not impact *nlp-29* expression (Zhu et al., 2023). Collectively, our findings support the notion that distinct non-neural molecular mechanisms may be underlying different dimensions of neuronal aging, even within an individual neuron.

2.7 ALM sensory neurons exhibit ectopic branching in response to loss-of-function mutation in *dpy-5* or *col-120*, but PLM neurons do not

To determine whether the regulatory role of skin collagens in neuron structural integrity is specific to certain neuron populations, we examined two additional sub-types of cutaneous sensory neurons in *C. elegans*: ALM and PLM touch receptor neurons, which are crucial for the perception of gentle touch (Corsi et al., 2015). Intriguingly, both *dpy-5(e907)* and *col-120(sy1526)* animals exhibited an increase in ectopic, aberrant branching from ALM anterior neurites at D3 when compared to CT animals, while PLM neurons showed no morphological abnormalities (Figure 5b-f). This discrepancy indicates that the regulatory role of examined collagens in neuritic branching may not extend uniformly across all cutaneous sensory neurons, suggesting that certain neuron sub-types may possess unique features rendering them particularly vulnerable to the effects of skin collagen loss during aging.

2.8 RIG-3/IgSF in interneurons acts upstream of epidermal collagens to regulate excessive PVD dendritic branching in aging

Next, we explored the downstream mechanisms by which collagen genes regulate PVD dendritic integrity during aging. In *C. elegans*, the polarized structure of epidermal cells

263 segregates apically secreted cuticular collagens from basement membrane collagens
264 anatomically and functionally (Chisholm & Xu, 2012), making direct interaction between COL-
265 120 or DPY-5 and sensory neurons (located on the basal side of the epidermis) unlikely. Thus,
266 the age-related decline in these collagens may contribute to neuronal aging through indirect
267 mechanisms, potentially involving cell signaling rather than direct structural support. To test
268 this hypothesis, we first examined several neuronal cell surface receptors using adulthood-
269 specific RNAi. We found that knockdown of *ina-1*, *pat-2* or *rig-3* led to early-onset excessive
270 dendritic branching in PVD (Figure 6a, Figure S7a-c). While *ina-1* and *pat-2* (both α-integrins)
271 are widely expressed, *rig-3*, encoding an Immunoglobulin Superfamily (IgSF) protein, is
272 expressed selectively in a small set of neurons but notably absent in PVD (Babu et al., 2011;
273 Taylor et al., 2021). This selective expression pattern makes *rig-3* a particularly intriguing
274 candidate for a non-cell-autonomous role in regulating PVD morphology. Analysis of *rig-*
275 *3(ok2156)* mutants confirmed our RNAi findings of early-onset excessive dendritic branching
276 but showed that *rig-3* mutation does not significantly impact PVD morphogenesis during
277 development (Figure 6b, Figure S7d-f).

278 We then conducted a rescue experiment using a pan-neuronal promoter to drive wild-type *rig-3*
279 expression in *rig-3(ok2156)*, fully restoring normal PVD dendritic branching (Figure 6c, Figure
280 S7g). Pan-neuronal overexpression of *rig-3* also significantly suppressed excessive branching
281 in aged animals (Figure 6f), similar to the effects of *col-120* or *dpy-5* overexpression (Figure 4).
282 Since *rig-3* is not detected in PVD, we sought to identify the specific neuron(s) through which it
283 acts. *rig-3* is highly expressed in interneurons, particularly in AVA, where it regulates
284 locomotion by modulating neuropeptide release from AVA, which in turn influences sensory
285 neurons connected to AVA (Bhardwaj et al., 2020). Notably, PVD axon also synapses with AVA
286 (White et al., 1986), leading us to hypothesize that RIG-3 may regulate PVD dendritic integrity
287 from AVA. Using the *nmr-1* promoter, which is active in fewer than 10 neuron subsets—
288 primarily interneurons including AVA, AVD, AVE and PVC, all of which also endogenously
289 express *rig-3* (Figure. S7i) (Brockie et al., 2001; Taylor et al., 2021), we conducted a rescue
290 experiment in *rig-3(ok2156)*. This fully rescued the excessive branching phenotype, suggesting
291 *rig-3* non-cell-autonomously regulates PVD dendritic branching from within this small set of
292 interneurons.

To determine if *rig-3* mediates the effects of skin collagens on PVD branching, we performed adulthood RNAi of *rig-3* in *col-120* or *dpy-5* mutants and found that it did not further enhance excessive branching in collagen mutants, suggesting *rig-3* functions in the same pathway as *dpy-5* and *col-120* in regulating PVD dendritic integrity during aging (Figure 6e, Figure S7j). Further epistasis analysis surprisingly revealed that *rig-3* overexpression's beneficial effect on branching in aged animals was completely blocked by *col-120* or *dpy-5* mutations (Figure 6f, Figure S7k). Conversely, *col-120* or *dpy-5* overexpression's effects remained even with *rig-3* mutation (Figure 6g-h, Figure S7l-m). Contrary to our expectations, these data suggest that neuronal RIG-3 likely functions upstream of collagens in maintaining PVD dendritic health over the course of aging.

2.9 Beneficial effect of COL-120 on PVD dendritic integrity requires DAF-16/FOXO

To further explore downstream pathways of skin collagen genes, we analyzed transcriptomic data (GSE19310) comparing wild-type animals and *dpy-10(e128)* mutants, another cuticular collagen mutation associated with early-onset excessive PVD branching (Figure S4). KEGG pathway analysis of differentially expressed genes in *dpy-10(e128)* revealed significant downregulation in several signaling pathways, including FOXO signaling (Figure S7n). We sought to examine potential interactions between collagen genes and *daf-16/FOXO*, focusing on *col-120*, given its stronger effect in suppressing excessive branching when overexpressed (Figure 4). We found that *daf-16(mu86)* mutation completely suppressed the beneficial effect of epidermis-specific *col-120* overexpression (Figure S7o-p). Since *col-120* overexpression was driven by the *col-19* promoter specifically in adulthood, rather than by its endogenous promoter, it is unlikely that the observed effect involves *daf-16* regulation of *col-120* expression. Additionally, previous studies show that *col-19* transcription is unaffected by *daf-2* or *daf-16* (Ewald et al., 2015; Uno et al., 2013), indicating that the effect observed with *daf-16* mutation is unlikely due to reduced expression of *col-19p::col-120* either. Notably, the suppression effect caused by *daf-16* mutation in *col-120* overexpression animals does not appear to result from the reduced lifespan caused by *daf-16* mutation. This interpretation is supported by the observation that D7 animals with *daf-16(mu86)* and *col-120* overexpression displayed branching levels more comparable to age-matched CTs, unlike the significant difference observed between D7 CT and D7 *daf-16(mu86)* single mutants (Figure 1h, Figure

323 S1g). Together, these results suggest that *daf-16*/FOXO may act downstream of *col-120* in
324 regulating PVD dendritic branching during aging.

325 **3. DISCUSSION**

326 Our study demonstrates that age-related reduction in epidermal collagen drives both structural
327 and functional changes of sensory neuron aging process. Interestingly, the impacts exhibit
328 selectivity, manifested at two levels: firstly, collagen reduction does not contribute to neuritic
329 beading in aging neurons, pointing to a phenotype-specific effect; secondly, their role is
330 confined to regulating branching integrity in specific sub-types of cutaneous sensory neurons,
331 highlighting a cell-type-targeted manner in neuron-epidermal interactions. Combined with our
332 previous findings (E et al., 2018), these results suggest that various molecular cues from non-
333 neural tissues during aging may trigger distinct neuronal aging mechanisms. Given that the
334 investigated collagens are secreted to the apical surface of the epidermis, their influence on
335 sensory neuron aging likely occurs via indirect mechanisms, rather than direct structural
336 support for neuronal structures. Unexpectedly, we identify RIG-3/IgSF in interneurons as an
337 upstream partner of skin collagens, coordinating neuronal homeostasis during aging. Notably,
338 the protective effect of collagen overexpression requires DAF-16/FOXO, but independent of its
339 role in lifespan regulation. Taken together, our findings suggest that the regulatory role of skin
340 collagens is mediated through an intricate, bi-directional communication processes between
341 neurons and epidermal cells, emphasizing the need for a paradigm shift towards exploring
342 multi-tissue strategies to comprehensively address the complexities of neuronal aging.

343 Although age-related declines in collagen production in various tissues have been well-
344 documented, its impact on the nervous system during aging remains underexplored. One
345 study reported that aged mice lacking COL6A1, a ubiquitously expressed collagen VI gene,
346 exhibited more severe deficits in motor coordination and spatial memory compared to age-
347 matched WT animals (Cescon et al., 2016). Our current study extends this area by
348 demonstrating that non-basement membrane collagens, particularly those from non-neural
349 tissues, play a distinctive regulatory role in maintaining neuronal structure and function during
350 aging. While our data suggest that DAF-16/FOXO mediates COL-120's effects on PVD
351 dendritic health, questions remain about whether DAF-16 acts within epiderma cells, whether

352 COL-120 engages additional signaling pathways that interact with DAF-16 elsewhere, and
353 which specific DAF-16 target genes are involved. Importantly, changes in key collagen genes
354 like *col-120* could broadly alter extracellular matrix (ECM) composition (Teuscher et al., 2024)
355 or influence signaling pathways, such as Wnt and TGF-β, as seen with *dpy-10* (Figure S7). In
356 fact, such extensive downstream effects may complicate the rescue of PVD excessive
357 branching phenotype in *col-120* or *dpy-5* mutants, as observed in this study, even with
358 endogenous promoters, as compensatory responses induced by collagen mutations could
359 interfere with attempts to fully restore normal function.

360 An unexpected finding from our study is the role of RIG-3/IgSF in interneurons as an upstream
361 partner of skin collagens in modulating PVD dendritic branching. Our data suggest that RIG-3
362 acts from interneurons, likely adjacent to PVD, yet the beneficial effects of *rig-3* overexpression
363 are blocked by the loss of skin collagens. This observation implies a signaling loop between
364 neurons and epidermal cells, rather than a simple neuron-neuron interaction, in the regulation
365 of neuronal aging. RIG-3 shares homology with mammalian neural cell adhesion molecule 1
366 (NCAM1), also an IgSF protein (Babu et al., 2011). Studies in a rat sciatic nerve injury model
367 have shown that NCAM1 on axonal membrane is essential for axonal fasciculation during
368 nerve regeneration, requiring interaction between extracellular collagen VI and the fibronectin
369 type III (FNIII) domain of NCAM1 (Sun et al., 2022). While RIG-3 also contains a FNIII domain
370 (Babu et al., 2011), the segregation of cuticular collagens to the epidermal apical surface
371 makes direct interaction with COL-120 or DPY-5 unlikely. Notably, RIG-3 can function as either
372 a cell surface or secreted protein (Babu et al., 2011); future studies may clarify whether its
373 secretion is required for its role in regulating PVD branching and assess its potential to act
374 over long distances.

375 Excessive branching in aging peripheral neurons is a conserved phenomenon. For example,
376 elderly humans with sensory neuropathy exhibit increased branching of epidermal nerve fibers
377 in the proximal thigh compared to healthy controls (Lauria et al., 1999). Our time-lapse imaging
378 revealed that excessive high-order dendritic branches in PVD neurons are enriched with F-
379 actin but lack microtubules, indicating high structural plasticity, much like dendritic spines,
380 known to affect neuronal signaling and synaptic plasticity. Therefore, it is tempting to speculate
381 that increased branching observed in aging reflects a compensatory plasticity for future

382 neurodegeneration at more advanced ages. Mechanotransduction may play a role in this
383 phenomenon. As *C. elegans* age, their cuticle becomes stiffer, while the ECM weakens,
384 reducing resistance to mechanical stress. Studies have shown that *col-120* expression can be
385 upregulated in response to mild mechanical compression, and loss of *col-120* decreases
386 cuticle mechanical resistance, particularly in long-lived *daf-2* mutants, suggesting a feedback
387 loop between ECM homeostasis and mechanotransduction (Rahimi et al., 2022; Teuscher et
388 al., 2024). Mechanosensitive sodium channels, such as MEC-10, UNC-8, DEL-1, and DEGT-1,
389 are localized to PVD dendritic branches and are essential for proprioceptive and
390 mechanonociceptive signaling (Tao et al., 2019). Age-related collagen loss could compromise
391 ECM stability, allowing cumulative mechanical stress to alter channel sensitivity over time and,
392 in turn, influence dendritic branching through modified sensory feedback to mechanical cues.
393 This effect may ultimately contribute to compensatory branching, inadvertently engaging
394 sensorimotor networks beyond their usual functional scope.

395 During nervous system development, transmembrane and extracellular proteins are crucial for
396 shaping neuronal structure and guiding migration. Proteins such as SAX-7/L1CAM, MNR-1,
397 and DMA-1 (transmembrane LRR protein) have been extensively studied for their roles in PVD
398 dendritic morphogenesis; however, deficiencies in these proteins primarily affect 1°- 4°
399 dendritic branches and do not contribute to excessive higher-order branching (Dong et al.,
400 2013; Salzberg et al., 2013). Additionally, we did not observe a clear link between abnormal
401 dendrite overlapping, often due to self-avoidance defects (Kravtsov et al., 2017; Oren-Suissa
402 et al., 2010), and excessive branching either during aging or in collagen mutants. These
403 observations suggest that the molecular mechanisms responsible for neuron morphogenesis in
404 development may be distinct from those driving neuron structural deterioration in aging.

405 Our findings indicate that polymodal sensory neurons can undergo multiple, distinct
406 morphological changes during aging, each corresponding to specific functional declines. In
407 PVD neurons, simultaneous excessive dendritic branching and dendritic beading are rare,
408 suggesting that animals may avoid experiencing major declines in both harsh touch function
409 and proprioception concurrently. The current study combined with our previous research (E et
410 al., 2018) indicate that within multifunctional neurons, certain structures and functions may be

411 selectively vulnerable to aging, likely driven by distinct non-neural signals. The question of
412 whether polymodal neurons prioritize one function over another remains unanswered.

413 On a broader scale, neurons across different regions exhibit varying susceptibility or resistance
414 to aging, leading to differences in the onset timing and progression of neurodegenerative
415 processes. This selective vulnerability is commonly observed in both normal aging and age-
416 related neurodegenerative diseases, and evident across species, including *C. elegans*. For
417 instance, ALM, PLM, and PVD neurons age at different rates (E et al., 2018) and respond
418 differently to the same skin-derived aging cues. Given that each neuron class/sub-type has a
419 unique gene expression profile, future research should investigate whether these molecular
420 signatures dictate responsiveness to non-neural or extracellular aging cues, contributing to
421 selective vulnerability.

422 4. MATERIALS AND METHODS

423 4.1 *C. elegans* Strains and Maintenance

424 *C. elegans* strains were maintained at 20°C, or as otherwise indicated, on Nematode Growth Medium
425 (NGM) plates seeded with *E. coli* OP50. Only hermaphrodites were used for data generating
426 experiments. For age-synchronized progeny, plates with gravid hermaphrodites were bleached to
427 eliminate microbes, and animals were transferred to NGM plates containing 100 μM 5'
428 fluorodeoxyuridine (FUDR) (VWR, 76345-984) at the mid- or late-L4 stage to prevent egg hatching. Day
429 1 of adulthood (D1) was defined as 24 hours post-L4. Given the potential confounding effects of FUDR
430 on aging (Feldman et al., 2014; Van Raamsdonk & Hekimi, 2011), key experiments were repeated
431 without FUDR, moving animals onto fresh plates daily until D5, every two days thereafter. FUDR-free
432 experiments are noted in figure legends. See Table S3 for strain information.

433 4.2 DNA Constructs and Generation of Transgenes

434 DNA expression constructs were generated using Gateway cloning technology (ThermoFisher), with
435 details in Table S4. Primers were acquired from Millipore and ThermoFisher (Table S5). Transgenic
436 animals were generated by microinjection, with plasmid DNAs used at 10-100 ng/μL, co-injection
437 marker *ttx-3p::RFP* or *ttx-3p::GFP* at 50 ng/μL (Tables S3, S4). At least two independent transgenic
438 lines were analyzed per construct. Promoters used include—*dpy-5p* (-854 bp from start codon), *col-*
439 *120p* (-348 bp), *nmr-1p* (-1104 bp), *dpy-7p* (-304 bp), *col-19p* (-649 bp), and *unc-33p* (-1974 bp).

440 **4.3 Fluorescent Microscopy**

441 Neurons were visualized using fluorescent reporters and phenotyped on a Zeiss Axio Imager M2 using
442 0.5-1% M9 dilution of 1-phenoxy-2-propanol (Fisher) for immobilization. Confocal images were taken on
443 a Leica SP8 with Z-stack (0.5-1µm/slice) at 63X magnification, using polystyrene beads (Polysciences,
444 00876-15) for immobilization.

445 **4.4 Quantification of Neuron Morphological Defects**

446 *wdIs51(F49H12.4::GFP)* (Smith et al., 2010) was used to visualize PVD neurons. Excessive dendritic
447 branching was quantified by counting 5° and 6° branches, identified within 'menorah' structures (Figure
448 1b). 5° and 6° branches for each animal were counted for either PVDL or PVDR for either the dorsal or
449 ventral side, depending on which was clearly visible during the imaging session. PVD dendritic beading
450 phenotype was assessed by counting bead- or bubble-like structures along the dendrites of either
451 PVDL or PVDR across the entire dendritic tree. Animals with ≥ 10 beads across ≥ 5 menorahs were
452 considered positive for degeneration (E et al., 2018). Severity scoring: in Figure 5a, animals with 0-10
453 beading structures was scored as normal, 10-20 as mild, 20-50 as moderate, and >50 as severe; in
454 Figure S1b, a finer scale was used: score 1 for 0-10 structures, 2 for 10-20, 3 for 20-30, 4 for 30-50, 5
455 for 50-100, 6 for 100-200, and 7 for over 200. *ser-2(3)p::mCherry-PH* was used to visualize PVD
456 dendritic membrane structures with respect to F-actin dynamics. For *rig-3* mutants, *ser-2(3)p::GFP*
457 *(lxyEx77)* was constructed to visualize PVD neurons due to challenges in crossing *rig-3(ok2156)X* with
458 *wdIs51X*. *ser-2(3)p::GFP(lxyEx77)* animals had larger body size than *wdIs51*, likely due to genetic
459 background differences, which may account for the branching number variation at D1 between the two
460 reporter strains.

461 *zdIs5(mec-4p::GFP)* was used to visualize ALM and PLM neurons, and the number of ectopic branches
462 sprouting from their main neurites were counted.

463 For each experimental group, a minimum of three replicates of 30 animals, or indicated otherwise, were
464 quantified alongside a control group, with experimenters blinded to sample identity to minimize bias.

465 **4.5 PVD Function Analysis: Harsh Touch Response**

466 The measurement of the harsh touch response was conducted using a *mec-4(u253)* mutant
467 background with non-functional touch receptor neurons but intact PVD neuron functionality, as
468 previously described (E et al., 2018), with modifications to the scoring system. A score of 1 was given if

469 the animal moved over one body length, 0.5 if it moved between one-third and one body length, and 0 if
470 it moved less than one-third or not at all. Each animal underwent 10 trials with 10-15 minute intervals.
471 Cumulative scores ranged from 0 (severely impaired response) to 10 (optimal response).

472 **4.6 PVD Function Analysis: Proprioception**

473 Proprioceptive sensing specific to PVD neurons was assessed using a locomotion assay as described
474 previously (Tao et al., 2019; Tavernarakis et al., 1997) with some modifications. On the day of assay,
475 animals were transferred to fresh NGM plates seeded with OP50, one animal per plate, and allowed to
476 roam freely for 2-3 hours at 20°C, until sufficient tracks were made in the bacterial lawn. The plate was
477 then imaged using a digital camera attached to a Leica S9i stereomicroscope at 1X magnification.
478 Three independent replicates of 10 animals each were assayed for each group. A total of 100 randomly
479 selected wavelengths (distance between two adjacent peaks) and amplitudes (distance between peak
480 and wavelength, perpendicular to wavelength) were measured using Fiji. All measurements were used
481 in cases where animals had fewer than 100 measurements, with a minimum of 40 measurements per
482 animal. All measurements were normalized to the body lengths of individual animals and units were
483 converted to millimeters utilizing a reference slide. All animals subjected to proprioception assay were
484 also examined under the Zeiss to quantify PVD dendritic branching.

485 **4.7 RT-qPCR**

486 To quantify the change in expression level of collagens in aging, N2 WT animals at D1 and D7 were
487 collected, washed with M9 solution for three 30-minute washes, and total RNA was isolated with TRI
488 reagent (Millipore Sigma).

489 To test RNAi efficacy, 10-worm lysis method (Ly et al., 2015) was used to prepare lysates. Briefly, 10
490 worms cleaned in H_2O and placed in 1 µL of lysis buffer (0.25 mM EDTA, 5mM Tris pH 8., 0.5% Triton
491 X-100, 0.5% Tween-20, 1mg/mL proteinase K). Samples were lysed in a thermal cycler at 65°C for 15
492 minutes, 85°C for 1 minute, and stored at -80°C for at least 12 hours. An additional 1.5 µL of lysis buffer
493 was then added, and the cycle was repeated. Samples were treated with dsDNAse (ThermoFisher; 0.5
494 µL each of 10X buffer and dsDNAse, 1.5 µL ultrapure H2O) and incubated at 37°C for 15 minutes, 55°C
495 for 5 minutes, and 65°C for 1 minute, followed by reverse transcription.

496 Reverse transcription was performed with iScript Reverse Transcription Supermix for RT-qPCR
497 (BioRad). RT-qPCR was performed using either TaqMan Gene Expression Assays (ThermoFisher,
498 Ce02462726_m1, Ce02417736_s1, Ce02457574_g1) and iTaq Universal Probes Supermix (Bio-Rad)

499 or using designed primers (Table S5) and iTaq Universal SYBR Green (Bio-Rad). *ama-1* and *cdc-42*
500 were used as housekeeping controls. Primer efficiency was verified utilizing standard curve method.
501 Bio Rad CFX96 Touch Deep Well Real-time PCR Detection System was used to perform the qPCR and
502 relative mRNA levels were calculated using comparative ΔΔCT method.

503 **4.8 Lifespan Assay**

504 L4 animals were transferred to assay plates and scored daily. An animal was considered dead when it
505 no longer responded to gentle prodding with a platinum wire and displayed no pharyngeal pumping.
506 Lifespan was calculated from the time animals were first placed on the assay plates until they were
507 scored as dead. Animals that died due to protruding/bursting vulva, internal hatching, as well as
508 animals that crawled off the agar were censored. For lifespan assays examining collagen
509 overexpression strains, the PVD::GFP background strain (*wdIs51*) was used as the control.

510 **4.9 Time-lapse Imaging**

511 Imaging of PVD branches was done on the Leica SP8 using 2% agarose pads with polystyrene beads
512 for immobilization. Control animals *[ser2(3)p::mCherry-PH; ser2(3)p::GFP::UtrCH(lxyEx51)]* were
513 imaged at D1 and D9. Each session lasted 8 minutes with 2-minute intervals, and images were Z-stack
514 projections captured with a 63X objective in both red and green channels. Branch dynamics were
515 quantified in Fiji by measuring the length of individual higher-order branches at each time-point, and
516 actin dynamics were assessed by observing GFP-labeled actin movement.

517 **4.10 Adulthood-specific RNAi**

518 Feeding method was used to perform RNAi experiments (Conte et al., 2015). FUDR at a concentration
519 of 100 μM was externally added to RNAi plates following growth of the HT115 bacterial lawn. The RNAi
520 clones were obtained from the Vidal RNAi library (Horizon Discovery, Table S4) or amplified from cDNA
521 using PCR. The section of cDNA included for each RNAi clone are *dpy-5::L4440 (1)* (PELZ88: 210 bp
522 section downstream of *dpy-5* start codon) and *col-120::L4440 (1)* (PELZ45: 256 bp section downstream
523 of *col-120* start codon). These regions were selected to ensure RNAi specificity, confirmed by BLAST
524 search to ensure no homology with other collagen genes. Additional RNAi clones were also included:
525 *dpy-5::L4440 (2)* (PELZ48: 554 bp section 301 bp downstream of *dpy-5* start codon) and *col-*
526 *120::L4440 (2)* (PELZ46: 605 bp section 337 bp downstream of *col-120* start codon). All RNAi clones
527 were sequenced to verify their identities. Empty L4440 plasmid was used as a negative control. TJ356
528 *[zIs356 (daf-16p::daf-16a/b::GFP)]* animals with empty-vector or *daf-2* RNAi treatment were used as a

529 positive control: Successful RNAi condition was indicated by nuclear translocation of DAF-16::GFP in
530 *daf-2* RNAi-treated animals, while cytoplasmic localization indicated unsuccessful treatment.

531 **4.11 Gene expression datasets and pathway analysis**

532 Gene expression datasets (GSE176088, GSE19310) were obtained from the NCBI Gene Expression
533 Omnibus. Data were analyzed using GEO2R to identify differentially expressed genes (DEGs), with
534 criteria of log2-fold change ≥ 1.5 and a *p*-value < 0.05. KEGG enrichment analysis was performed using
535 the Database for Annotation, Visualization and Integrated Discovery (Sherman et al., 2022), applying
536 an FDR < 0.01 for statistical significance. The top 10 significant KEGG pathways were visualized in a
537 bubble graph, with the rich factor representing the proportion of DEGs within each pathway term.

538 **4.12 Statistical Analysis**

539 Data processing, statistical analyses, and graph plotting were performed with GraphPad Prism
540 software. Normality was assessed using the D'Agostino & Pearson test. For comparisons between
541 experimental and control groups, unpaired t-test for normally distributed data, and the Mann-Whitney
542 test for non-normally distributed data were used. When comparing three or more groups, either one-
543 way ANOVA or the Kruskal-Wallis test, followed by post-hoc analysis. Pearson's correlation test was
544 applied for correlation analyses. Log-Rank test was used to analyze lifespan data. Bar graphs display
545 the mean ± SEM for normally distributed data, and the median with interquartile range for non-normally
546 distributed data.

547 **ACKNOWLEDGMENTS**

548 We thank Bradey A. R. Stuart for assistance in molecular cloning and construction of
549 transgenic strains. Some strains were provided by the CGC, which is funded by NIH Office of
550 Research Infrastructure Programs (P40 OD010440).

551 **CONFLICT OF INTEREST**

552 The authors declare that the research was conducted in the absence of any commercial or
553 financial relationships that could be construed as a potential conflict of interest.

554 **FUNDING SUPPORT**

This work was supported by the Imagine More Award and Research Affairs Committee at the Medical College of Wisconsin, as well as Advancing a Healthier Wisconsin (AHW) Endowment project 5520482 titled Developing Innovative Translational Research Programs in Clinically Relevant Neurological Disorders.

AUTHOR CONTRIBUTIONS

L.E. conceived the project; L.E. and M.K. designed the experiments; M.K., L.E., S.G.W., A.L.F., and E.M. performed the experiments and collected the data; M.K., S.G.W. and L.E. analyzed and interpreted the data; M.K. and L.E. drafted the manuscript; M.K., S.G.W., A.L.F., E.M. and L.E. edited and proofread the manuscript.

DATA AVAILABILITY

The data that support the findings of this study are available from the corresponding author upon reasonable request.

REFERENCES

Babu, K., Hu, Z., Chien, S. C., Garriga, G., & Kaplan, J. M. (2011). The immunoglobulin super family protein RIG-3 prevents synaptic potentiation and regulates Wnt signaling. *Neuron*, *71*(1), 103-116. https://doi.org/10.1016/j.neuron.2011.05.034

Bhardwaj, A., Pandey, P., & Babu, K. (2020). Control of Locomotory Behavior of Caenorhabditis elegans by the Immunoglobulin Superfamily Protein RIG-3. *Genetics*, *214*(1), 135-145. https://doi.org/10.1534/genetics.119.302872

Brockie, P. J., Mellem, J. E., Hills, T., Madsen, D. M., & Maricq, A. V. (2001). The C. elegans glutamate receptor subunit NMR-1 is required for slow NMDA-activated currents that regulate reversal frequency during locomotion. *Neuron*, *31*(4), 617-630. https://doi.org/10.1016/s0896-6273(01)00394-4

Callisaya, M. L., Blizzard, L., Schmidt, M. D., McGinley, J. L., & Srikanth, V. K. (2010). Ageing and gait variability--a population-based study of older people. *Age Ageing*, *39*(2), 191-197. https://doi.org/10.1093/ageing/afp250

Cescon, M., Chen, P., Castagnaro, S., Gregorio, I., & Bonaldo, P. (2016). Lack of collagen VI promotes neurodegeneration by impairing autophagy and inducing apoptosis during aging. *Aging (Albany NY)*, *8*(5), 1083-1101. https://doi.org/10.18632/aging.100924

Chatzigeorgiou, M., Yoo, S., Watson, J. D., Lee, W. H., Spencer, W. C., Kindt, K. S., Hwang, S. W., Miller, D. M., Treinin, M., Driscoll, M., & Schafer, W. R. (2010). Specific roles for DEG/ENaC and TRP channels in touch and thermosensation in C. elegans nociceptors. *Nat Neurosci*, *13*(7), 861-868. https://doi.org/10.1038/nn.2581

Chisholm, A. D., & Hsiao, T. I. (2012). The Caenorhabditis elegans epidermis as a model skin. I: development, patterning, and growth. *Wiley Interdiscip Rev Dev Biol*, *1*(6), 861-878. https://doi.org/10.1002/wdev.79

Chisholm, A. D., & Xu, S. (2012). The Caenorhabditis elegans epidermis as a model skin. II: differentiation and physiological roles. *Wiley Interdiscip Rev Dev Biol*, *1*(6), 879-902. https://doi.org/10.1002/wdev.77

Conte, D., Jr., MacNeil, L. T., Walhout, A. J. M., & Mello, C. C. (2015). RNA Interference in Caenorhabditis elegans. *Curr Protoc Mol Biol*, *109*, 26 23 21-26 23 30. https://doi.org/10.1002/0471142727.mb2603s109

Corsi, A. K., Wightman, B., & Chalfie, M. (2015). A Transparent window into biology: A primer on Caenorhabditis elegans. *WormBook*, 1-31. https://doi.org/10.1895/wormbook.1.177.1

Dong, X., Liu, O. W., Howell, A. S., & Shen, K. (2013). An extracellular adhesion molecule complex patterns dendritic branching and morphogenesis. *Cell*, *155*(2), 296-307. https://doi.org/10.1016/j.cell.2013.08.059

E, L., Zhou, T., Koh, S., Chuang, M., Sharma, R., Pujol, N., Chisholm, A. D., Eroglu, C., Matsunami, H., & Yan, D. (2018). An Antimicrobial Peptide and Its Neuronal Receptor Regulate Dendrite Degeneration in Aging and Infection. *Neuron*, *97*(1), 125-138.e125. https://doi.org/10.1016/j.neuron.2017.12.001

Ewald, C. Y., Landis, J. N., Porter Abate, J., Murphy, C. T., & Blackwell, T. K. (2015). Dauer-independent insulin/IGF-1-signalling implicates collagen remodelling in longevity. *Nature*, *519*(7541), 97-101. https://doi.org/10.1038/nature14021

Faerman, I., Faccio, E., Calb, I., Razumny, J., Franco, N., Dominguez, A., & Podesta, H. A. (1982). Autonomic neuropathy in the skin: a histological study of the sympathetic nerve

fibres in diabetic anhidrosis. *Diabetologia*, *22*(2), 96-99. https://doi.org/10.1007/BF00254836

Feldman, N., Kosolapov, L., & Ben-Zvi, A. (2014). Fluorodeoxyuridine improves Caenorhabditis elegans proteostasis independent of reproduction onset. *PLoS One*, *9*(1), e85964. https://doi.org/10.1371/journal.pone.0085964

Goyala, A., & Ewald, C. Y. (2023). CRISPR-activated expression of collagen col-120 increases lifespan and heat tolerance. *MicroPubl Biol*, *2023*. https://doi.org/10.17912/micropub.biology.000730

Hicks, C. W., Wang, D., Windham, B. G., Matsushita, K., & Selvin, E. (2021). Prevalence of peripheral neuropathy defined by monofilament insensitivity in middle-aged and older adults in two US cohorts. *Sci Rep*, *11*(1), 19159. https://doi.org/10.1038/s41598-021-98565-w

Ishii, N., Fujii, M., Hartman, P. S., Tsuda, M., Yasuda, K., Senoo-Matsuda, N., Yanase, S., Ayusawa, D., & Suzuki, K. (1998). A mutation in succinate dehydrogenase cytochrome b causes oxidative stress and ageing in nematodes. *Nature*, *394*(6694), 694-697. https://doi.org/10.1038/29331

Jiang, N., Rasmussen, J. P., Clanton, J. A., Rosenberg, M. F., Luedke, K. P., Cronan, M. R., Parker, E. D., Kim, H. J., Vaughan, J. C., Sagasti, A., & Parrish, J. Z. (2019). A conserved morphogenetic mechanism for epidermal ensheathment of nociceptive sensory neurites. *Elife*, *8*. https://doi.org/10.7554/eLife.42455

Kaech, S., Parmar, H., Roelandse, M., Bornmann, C., & Matus, A. (2001). Cytoskeletal microdifferentiation: a mechanism for organizing morphological plasticity in dendrites. *Proc Natl Acad Sci U S A*, *98*(13), 7086-7092. https://doi.org/10.1073/pnas.111146798

Klass, M. R. (1977). Aging in the nematode Caenorhabditis elegans: major biological and environmental factors influencing life span. *Mech Ageing Dev*, *6*(6), 413-429. https://doi.org/10.1016/0047-6374(77)90043-4

Kravtsov, V., Oren-Suissa, M., & Podbilewicz, B. (2017). The fusogen AFF-1 can rejuvenate the regenerative potential of adult dendritic trees by self-fusion. *Development*, *144*(13), 2364-2374. https://doi.org/10.1242/dev.150037

Krimm, R. F., Davis, B. M., Noel, T., & Albers, K. M. (2006). Overexpression of neurotrophin 4 in skin enhances myelinated sensory endings but does not influence sensory neuron number. *J Comp Neurol*, *498*(4), 455-465. https://doi.org/10.1002/cne.21074

Lauria, G., Holland, N., Hauer, P., Cornblath, D. R., Griffin, J. W., & McArthur, J. C. (1999). Epidermal innervation: changes with aging, topographic location, and in sensory neuropathy. *J Neurol Sci*, *164*(2), 172-178. https://doi.org/10.1016/s0022-510x(99)00063-5

Lee, H., & Lee, S. V. (2022). Recent Progress in Regulation of Aging by Insulin/IGF-1 Signaling in Caenorhabditis elegans. *Mol Cells*, *45*(11), 763-770. https://doi.org/10.14348/molcells.2022.0097

Ly, K., Reid, S. J., & Snell, R. G. (2015). Rapid RNA analysis of individual Caenorhabditis elegans. *MethodsX*, *2*, 59-63. https://doi.org/10.1016/j.mex.2015.02.002

Oren-Suissa, M., Hall, D. H., Treinin, M., Shemer, G., & Podbilewicz, B. (2010). The fusogen EFF-1 controls sculpting of mechanosensory dendrites. *Science*, *328*(5983), 1285-1288. https://doi.org/10.1126/science.1189095

656 Rahimi, M., Sohrabi, S., & Murphy, C. T. (2022). Novel elasticity measurements reveal C.
657 elegans cuticle stiffens with age and in a long-lived mutant. *Biophys J*, *121*(4), 515-524.
658 https://doi.org/10.1016/j.bpj.2022.01.013
659 Salzberg, Y., Diaz-Balzac, C. A., Ramirez-Suarez, N. J., Attreed, M., Tecle, E., Desbois, M.,
660 Kaprielian, Z., & Bulow, H. E. (2013). Skin-derived cues control arborization of sensory
661 dendrites in Caenorhabditis elegans. *Cell*, *155*(2), 308-320.
662 https://doi.org/10.1016/j.cell.2013.08.058
663 Sandhu, A., Badal, D., Sheokand, R., Tyagi, S., & Singh, V. (2021). Specific collagens maintain
664 the cuticle permeability barrier in Caenorhabditis elegans. *Genetics*, *217*(3).
665 https://doi.org/10.1093/genetics/iyaa047
666 Sherman, B. T., Hao, M., Qiu, J., Jiao, X., Baseler, M. W., Lane, H. C., Imamichi, T., & Chang,
667 W. (2022). DAVID: a web server for functional enrichment analysis and functional
668 annotation of gene lists (2021 update). *Nucleic Acids Res*, *50*(W1), W216-W221.
669 https://doi.org/10.1093/nar/gkac194
670 Smith, C. J., Watson, J. D., Spencer, W. C., O'Brien, T., Cha, B., Albeg, A., Treinin, M., & Miller,
671 D. M. (2010). Time-lapse imaging and cell-specific expression profiling reveal dynamic
672 branching and molecular determinants of a multi-dendritic nociceptor in C. elegans. *Dev*
673 *Biol*, *345*(1), 18-33. https://doi.org/10.1016/j.ydbio.2010.05.502
674 Sun, J. H., Huang, M., Fang, Z., Li, T. X., Wu, T. T., Chen, Y., Quan, D. P., Xu, Y. Y., Wang, Y.
675 M., Yang, Y., & Zou, J. L. (2022). Nerve bundle formation during the promotion of
676 peripheral nerve regeneration: collagen VI-neural cell adhesion molecule 1 interaction.
677 *Neural Regen Res*, *17*(5), 1023-1033. https://doi.org/10.4103/1673-5374.324861
678 Takeuchi, H., Mizuno, T., Zhang, G., Wang, J., Kawanokuchi, J., Kuno, R., & Suzumura, A.
679 (2005). Neuritic beading induced by activated microglia is an early feature of neuronal
680 dysfunction toward neuronal death by inhibition of mitochondrial respiration and axonal
681 transport. *J Biol Chem*, *280*(11), 10444-10454. https://doi.org/10.1074/jbc.M413863200
682 Tao, L., Porto, D., Li, Z., Fechner, S., Lee, S. A., Goodman, M. B., Xu, X. Z. S., Lu, H., & Shen,
683 K. (2019). Parallel Processing of Two Mechanosensory Modalities by a Single Neuron in
684 C. elegans. *Dev Cell*, *51*(5), 617-631.e613. https://doi.org/10.1016/j.devcel.2019.10.008
685 Tavernarakis, N., Shreffler, W., Wang, S., & Driscoll, M. (1997). unc-8, a DEG/ENaC family
686 member, encodes a subunit of a candidate mechanically gated channel that modulates
687 C. elegans locomotion. *Neuron*, *18*(1), 107-119. https://doi.org/10.1016/s0896-
688 6273(01)80050-7
689 Taylor, S. R., Santpere, G., Weinreb, A., Barrett, A., Reilly, M. B., Xu, C., Varol, E., Oikonomou,
690 P., Glenwinkel, L., McWhirter, R., Poff, A., Basavaraju, M., Rafi, I., Yemini, E., Cook, S.
691 J., Abrams, A., Vidal, B., Cros, C., Tavazoie, S., Sestan, N., Hammarlund, M., Hobert,
692 O., & Miller, D. M. (2021). Molecular topography of an entire nervous system. *Cell*,
693 *184*(16), 4329-4347.e4323. https://doi.org/10.1016/j.cell.2021.06.023
694 Teuscher, A. C., Jongsma, E., Davis, M. N., Statzer, C., Gebauer, J. M., Naba, A., & Ewald, C.
695 Y. (2019). The in-silico characterization of the Caenorhabditis elegans matrisome and
696 proposal of a novel collagen classification. *Matrix Biol Plus*, *1*, 100001.
697 https://doi.org/10.1016/j.mbplus.2018.11.001
698 Teuscher, A. C., Statzer, C., Goyala, A., Domenig, S. A., Schoen, I., Hess, M., Hofer, A. M.,
699 Fossati, A., Vogel, V., Goksel, O., Aebersold, R., & Ewald, C. Y. (2024). Longevity
700 interventions modulate mechanotransduction and extracellular matrix homeostasis in C.
701 elegans. *Nat Commun*, *15*(1), 276. https://doi.org/10.1038/s41467-023-44409-2

Thacker, C., Sheps, J. A., & Rose, A. M. (2006). Caenorhabditis elegans dpy-5 is a cuticle procollagen processed by a proprotein convertase. *Cell Mol Life Sci*, *63*(10), 1193-1204. https://doi.org/10.1007/s00018-006-6012-z

Thein, M. C., McCormack, G., Winter, A. D., Johnstone, I. L., Shoemaker, C. B., & Page, A. P. (2003). Caenorhabditis elegans exoskeleton collagen COL-19: an adult-specific marker for collagen modification and assembly, and the analysis of organismal morphology. *Dev Dyn*, *226*(3), 523-539. https://doi.org/10.1002/dvdy.10259

Uno, M., Honjoh, S., Matsuda, M., Hoshikawa, H., Kishimoto, S., Yamamoto, T., Ebisuya, M., Yamamoto, T., Matsumoto, K., & Nishida, E. (2013). A fasting-responsive signaling pathway that extends life span in C. elegans. *Cell Rep*, *3*(1), 79-91. https://doi.org/10.1016/j.celrep.2012.12.018

Van de Walle, P., Geens, E., Baggerman, G., Jose Naranjo-Galindo, F., Askjaer, P., Schoofs, L., & Temmerman, L. (2019). CEH-60/PBX regulates vitellogenesis and cuticle permeability through intestinal interaction with UNC-62/MEIS in Caenorhabditis elegans. *PLoS Biol*, *17*(11), e3000499. https://doi.org/10.1371/journal.pbio.3000499

Van Raamsdonk, J. M., & Hekimi, S. (2011). FUdR causes a twofold increase in the lifespan of the mitochondrial mutant gas-1. *Mech Ageing Dev*, *132*(10), 519-521. https://doi.org/10.1016/j.mad.2011.08.006

White, J. G., Southgate, E., Thomson, J. N., & Brenner, S. (1986). The structure of the nervous system of the nematode Caenorhabditis elegans. *Philos Trans R Soc Lond B Biol Sci*, *314*(1165), 1-340. https://doi.org/10.1098/rstb.1986.0056

Wiesmeier, I. K., Dalin, D., & Maurer, C. (2015). Elderly Use Proprioception Rather than Visual and Vestibular Cues for Postural Motor Control. *Front Aging Neurosci*, *7*, 97. https://doi.org/10.3389/fnagi.2015.00097

Zhu, Y., Li, W., Dong, Y., Xia, C., & Fu, R. (2023). C. elegans Hemidesmosomes Sense Collagen Damage to Trigger Innate Immune Response in the Epidermis. *Cells*, *12*(18). https://doi.org/10.3390/cells12182223

FIGURE LEGENDS

Figure 1: Aging triggers the progressive development of excessive higher-order dendritic branching in PVD neurons

(a) Schematic diagram of PVD neuron in control (CT) animals [*F49H12.4::GFP(wdIs51)*]. Black boxes indicate regions imaged.

(b) A 'menorah' structure with orders of dendritic branching indicated.

(c) Representative images of anterior (Zone 1) and posterior (Zone 2) sections of PVD neuron at Day 1 (D1) and D9 of adulthood in CT animals. Blue and red boxes indicate zoomed in sections for Zone 1 and 2 respectively. Yellow and blue arrowheads indicate PVD soma and axon respectively. White and red arrowheads indicate 5° and 6° dendritic branches respectively. Scale bar = 20 μM. Mild autofluorescence of gut granules, a normal physiological feature in *C. elegans*, appears as small punctate structures in the background.

(d-e) Quantification of 5° *(d)* and 6° *(e)* dendrites during aging in CT animals (D1: n = 70, D3: n = 50, D6: n = 98, D9: n = 100).

(f-g) 5° *(f)* and 6° *(g)* dendrites in CT animals cultured at different temperatures (D6 15° C: n = 36, D6 20° C: n = 39, D6 25° C: n = 41, D9 15° C, 20° C, 25° C: n = 20).

(h) 5° dendrites in CT and *daf-16(mu86)* mutant animals (CT D3: n = 51, CT D7: n = 70, *daf-16* D3: n = 47, *daf-16* D7: n = 46). Experiments performed without FUDR.

(i-p) Number of 5° dendrites normalized to number of 4° dendrites or menorahs. PVD soma was used as a reference point to determine anterior and posterior sections. *(i)* D3: n = 21, D7: n = 19. *(j)* D3: n = 22, D7: n = 39. *(k)* D3: n = 21, D7: n = 19. *(l)* D3: n = 22, D7: n = 39. *(m-p)* D3: n = 43, D7: n = 58. Experiments performed without FUDR.

(q) Representative time-lapse images of actin dynamics in higher-order dendritic branches during an 8-minute session at 2-minute intervals in D1 and D9 CT animals [*ser-2(3)p::GFP::UtrCH + ser-2(3)p::mCherry-PH(lxyEx51)*]. mCherry::PH was used to visualize the membrane structures of PVD dendrites. Yellow arrows indicate 2° and 3° dendrites. White and red arrowheads indicate 5° and 6° dendrites, with asterisks indicating dendrites where a dynamic actin remodeling event occurs. Scale bar = 10 μm.

(r-s) Changes in the length of higher-order dendrites relative to their initial lengths were tracked using time-lapse imaging data obtained from D1*(r)* and D9*(s)* CT animals as in *(q)*. Measurements were taken for 5° and 6° dendrites branching from 4° and 5° dendrites, respectively, with each line representing a single higher-order dendrite. *n* (animals imaged) = 3/group.

(t) Absolute change in branch length over 8 minutes in D1 and D9 CT animals (measurements from *(r-s)*), with each point representing a higher-order dendrite. n = 3/group.

* $p<0.05$, *** $p<0.001$, **** $p<0.0001$.

Figure 2: Aging-associated excessive dendritic branching in PVD neurons correlates with proprioceptive deficits

(a) Representative images of movement tracks of CT animals at D3 and D9. Scale bar = 500 μM.

(b-c) Mean amplitude *(b)* and wavelength *(c)* measured from 100 tracks per animal in CT animals. Normalized for animal body length (D3: n = 42, D7: n = 36).

(d-e) Variability in amplitude *(d)* and wavelength *(e)* measured via coefficient of variability (CV) from 100 tracks per animal in CT animals (D3: n = 42, D7: n = 36).

(f-i) Correlation between proprioception measurements and number of PVD 5° dendritic branches. Each data point represents an individual animal.

**** $p<0.0001$. All experiments in this figure performed without FUDR.

Figure 3: Loss of epidermal collagen leads to early-onset of aging-associated excessive branching and proprioceptive deficit

(a) Domain structures of COL-120 and DPY-5, with key features annotated. Adapted from CeCoIDB (Teuscher et al., 2019).

(b-c) Representative images of excessive PVD dendritic branching in *dpy-5(e907)* mutant *(b)* and *col-120(sy1526)* mutant *(c)* animals at D3. White and red arrowheads indicate 5° and 6° dendrites respectively. Scale bar = 50 μM.

(d) Quantification of 5° dendrites in CT (n = 50), *dpy-5* mutant (n = 50), and endogenous promoter-driven rescue in *dpy-5* mutant (n = 49).

(e) 5° dendrites in CT, *dpy-5* mutant, and epidermis-specific rescue in *dpy-5* mutant (driven by *dpy-7p*; line 1) (n = 60 for all groups).

(f) 5° dendrites in CT (n = 40), *col-120* mutant (n = 38), and endogenous promoter-driven rescue in *col-120* mutant (n = 38).

(g) 5° dendrites in CT (n = 82), *col-120* mutant (n = 100), and epidermis-specific rescue in *col-120* mutant (driven by *dpy-7p* and *col-19p*; line 1) (n = 55).

(h) 5° dendrites in empty vector (EV) (n = 70) and *dpy-5* RNAi treated animals (n = 88; RNAi clone 1).

(i) 5° dendrites in EV (n = 70) and *col-120* RNAi treated animals (n = 70; RNAi clone 1).

(j) Representative images of movement tracks of D3 CT, D9 CT and D3 *col-120(sy1526)* animals. Scale bar = 500 μM.

(k-l) Mean amplitude *(k)* and wavelength *(l)* measured from 100 tracks per animal for D3 CT (n = 28), D9 CT (n = 51), and D3 *col-120* mutant (n = 25). Normalized for animal body length.

ns- not significant, * $p<0.05$, ** $p<0.005$, *** $p<0.001$, **** $p<0.0001$.

Figure 4: Adulthood-specific overexpression of collagen genes mitigates aging-associated excessive dendritic branching in PVD neurons

(a) Quantification of 5° dendrites in CT (n = 46) and *dpy-5* epidermis-specific overexpression driven by *col-19p* (n = 50).

(b) 5° dendrites in CT (n = 53) and *col-120* epidermis-specific overexpression driven by *col-19p* (n = 54; line 2).

(c-d) Lifespan comparison between CT (n = 100) and *dpy-5* epidermis-specific overexpression driven by *col-19p* (n = 100) *(c)*, as well as CT (n = 100) and *col-120* epidermis-specific overexpression driven by *col-19p* (n = 100; line 1) *(d)*. No statistical significance compared to CT. Additional replicates in Figure S6. Experiments performed without FUDR.

*** $p<0.001$, **** $p<0.0001$.

Figure 5: Selective impact of epidermal collagens on the aging process of sensory neurons

(a) Quantification of PVD dendritic beading in control (CT, n = 29), *dpy-5(e907)* (n = 26), and *col-120(sy1526)* (n = 29). Scored based on severity of beading phenotype.

(b) Schematic diagram of ALM and PLM neuron, with a representative image of the ALM neuron in CT [*mec-4p::GFP(zdIs5)*] animals at D3 and D11. Scale bar = 50 μM. White and yellow arrowheads indicate the ectopic branching from ALM anterior neurite and the ALM soma respectively.

(c-d) Ectopic branches in ALM *(c)* and PLM neuron *(d)* in CT (n = 78) and *dpy-5(e907)* (n = 131). Number of ectopic branches observed per animal is indicated.

(e-f) Ectopic branches in ALM *(e)* and PLM neuron *(f)* in CT (n = 67) and *120(sy1526)* (n = 81).

ns- not significant, * $p<0.05$, **** $p<0.0001$.

Figure 6: RIG-3/IgSF acts as upstream of epidermal collagens to regulate PVD dendritic integrity in aging

(a) Quantification of 5° dendrites in empty vector (EV) and *rig-3* RNAi treated CT animals at D3. (n = 84).

(b) 5° dendrites in CT (n = 91) (*ser-2(3)p::GFP(lxyEx77)*, see Methods) and *rig-3(ok2156)* mutant (n = 90).

(c) 5° dendrites in CT (n = 37), *rig-3(ok2156)* (n = 40), and pan-neuronal rescue (driven by *unc-33p*) in *rig-3(ok2156)* (n = 37).

(d) 5° dendrites in CT (n = 41), *rig-3(ok2156)* (n = 46), and interneuron rescue (driven by *nmr-1p*) in *rig-3(ok2156)* (n = 37).

(e) 5° dendrites in *dpy-5(e907)* mutant animals treated with EV (n = 84) or *rig-3* RNAi (n = 85), as well as in *col-120(sy1526)* mutant animals treated with EV (n = 88) or *rig-3* RNAi (n = 86).

(f) 5° dendrites in CT (n = 76), *rig-3* pan-neuronal overexpression driven by *unc-33p* (n = 57), *rig-3* overexpression in *dpy-5(e907)* mutant background (n = 10), and *rig-3* overexpression in *col-120(sy1526)* mutant background (n = 37).

(g) 5° dendrites in CT (*ser-2(3)p::GFP(lxyEx77)*) (n = 30), *dpy-5* epidermis-specific overexpression driven by *col-19p* (n = 22), and *dpy-5* overexpression in *rig-3(ok2156)* mutant background (n = 18).

(h) 5° dendrites in CT (n = 10), *col-120* epidermis-specific overexpression driven by *col-19p* (n = 19; line 1), and *col-120* overexpression (line 1) in *rig-3(ok2156)* mutant background (n = 20).

ns-not significant, * $p<0.05$, ** $p<0.005$, *** $p<0.001$, **** $p<0.0001$.

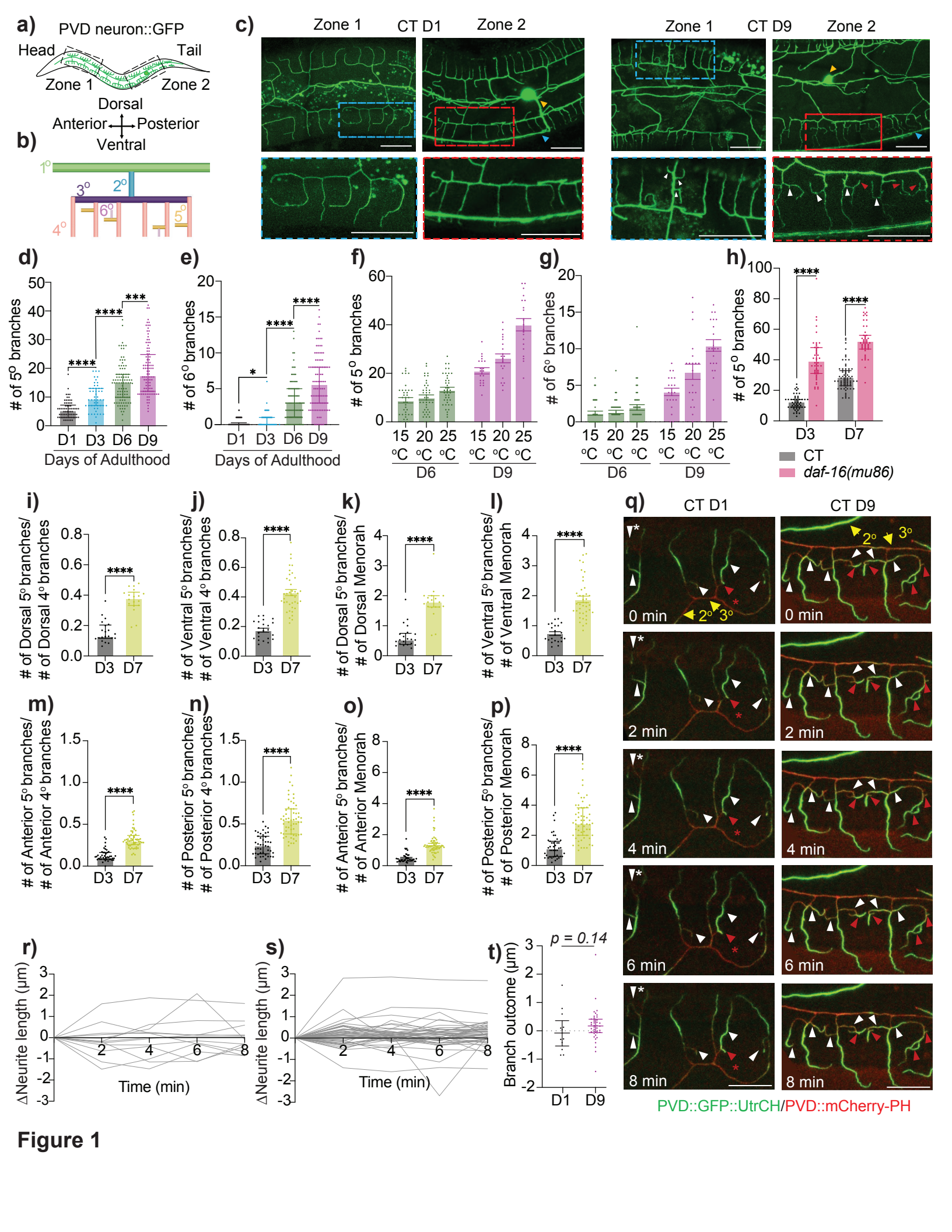
a)
PVD neuron::GFP
Head
Tail
Zone 1
Zone 2
Dorsal
Anterior
Posterior
Ventral
b)
1°
2°
3°
4°
5°
6°
c)
Zone 1
CT D1
Zone 2
Zone 1
CT D9
Zone 2
d)
# of 5° branches
Days of Adulthood
D1 D3 D6 D9
e)
# of 6° branches
Days of Adulthood
D1 D3 D6 D9
f)
# of 5° branches
15 °C 20 °C 25 °C
D6 D9
g)
# of 6° branches
15 °C 20 °C 25 °C
D6 D9
h)
# of 5° branches
D3 D7
CT
daf-16(mu86)
i)
# of Dorsal 5° branches/ # of Dorsal 4° branches
j)
# of Ventral 5° branches/ # of Ventral 4° branches
k)
# of Dorsal 5° branches/ # of Dorsal Menorah
l)
# of Ventral 5° branches/ # of Ventral Menorah
m)
# of Anterior 5° branches/ # of Anterior 4° branches
n)
# of Posterior 5° branches/ # of Posterior 4° branches
o)
# of Anterior 5° branches/ # of Anterior Menorah
p)
# of Posterior 5° branches/ # of Posterior Menorah
D3 D7
q)
CT D1
CT D9
0 min
2 min
4 min
6 min
8 min
PVD::GFP::UtrCH/PVD::mCherry-PH
r)
ΔNeurite length (μm)
Time (min)
s)
ΔNeurite length (μm)
Time (min)
t)
p = 0.14
Branch outcome (μm)
D1 D9

Figure 1

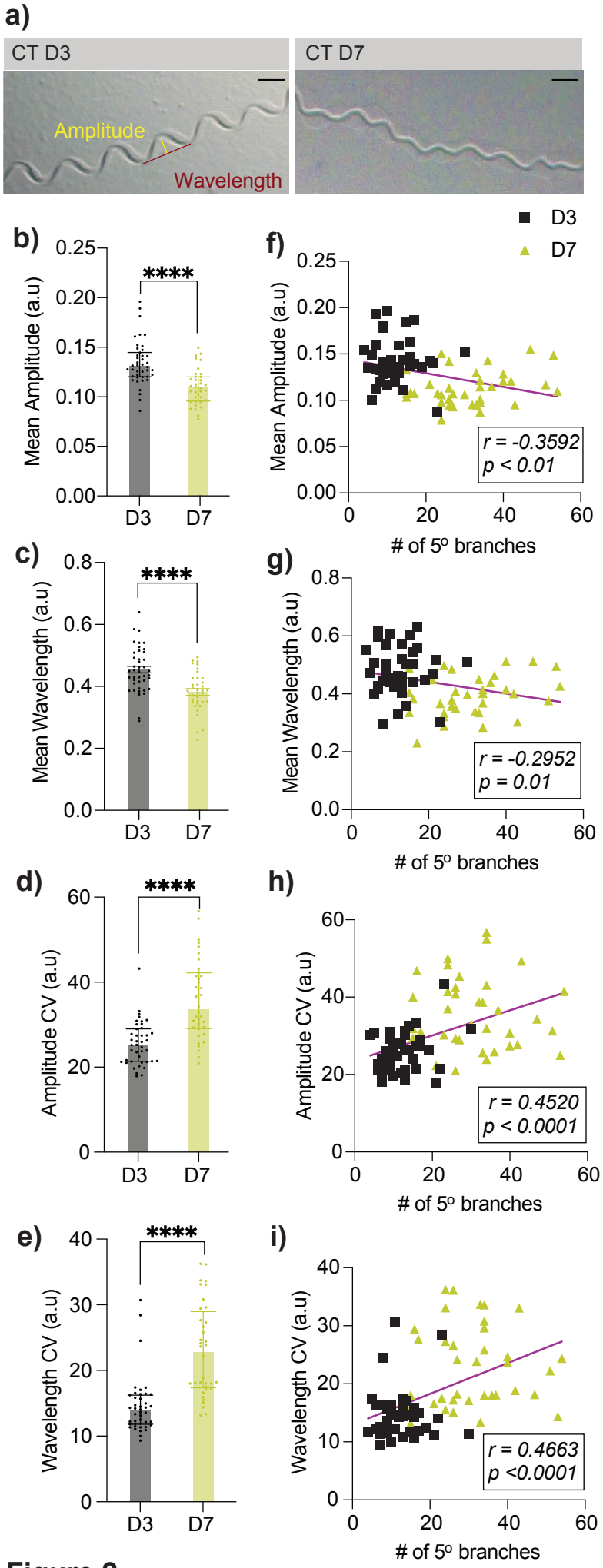
a)
CT D3
CT D7
Amplitude
Wavelength
b)
Mean Amplitude (a.u)
****
D3
D7
c)
Mean Wavelength (a.u)
****
d)
Amplitude CV (a.u)
****
e)
Wavelength CV (a.u)
****
f)
D3
D7
Mean Amplitude (a.u)
r = -0.3592
p < 0.01
# of 5º branches
g)
Mean Wavelength (a.u)
r = -0.2952
p = 0.01
h)
Amplitude CV (a.u)
r = 0.4520
p < 0.0001
i)
Wavelength CV (a.u)
r = 0.4663
p <0.0001

Figure 2

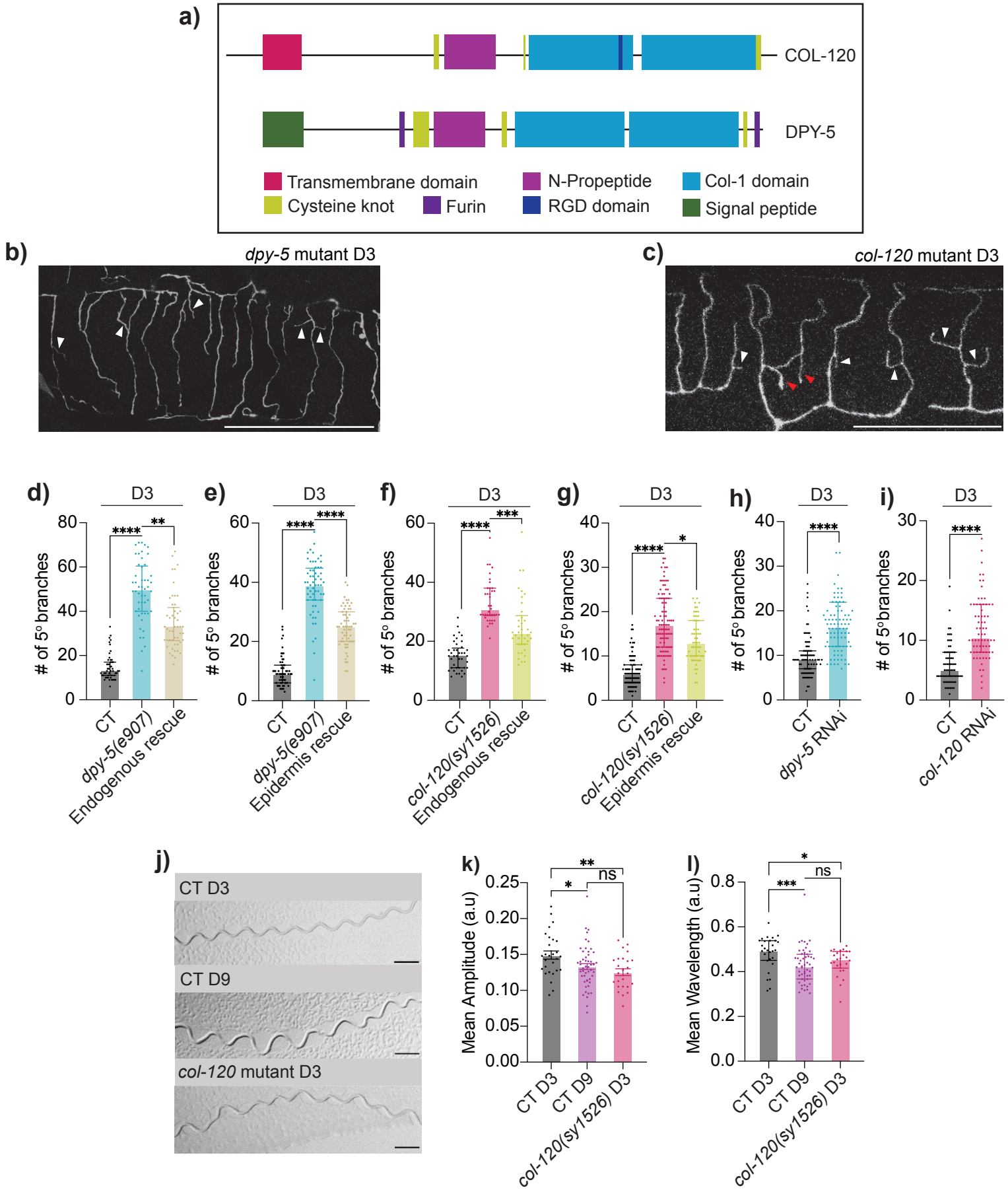
a)
COL-120
DPY-5
Transmembrane domain
Cysteine knot
Furin
N-Propeptide
RGD domain
Col-1 domain
Signal peptide
b)
dpy-5 mutant D3
c)
col-120 mutant D3
d)
D3
# of 5° branches
CT
dpy-5(e907)
Endogenous rescue
e)
D3
# of 5° branches
CT
dpy-5(e907)
Epidermis rescue
f)
D3
# of 5° branches
CT
col-120(sy1526)
Endogenous rescue
g)
D3
# of 5° branches
CT
col-120(sy1526)
Epidermis rescue
h)
D3
# of 5° branches
CT
dpy-5 RNAi
i)
D3
# of 5° branches
CT
col-120 RNAi
j)
CT D3
CT D9
col-120 mutant D3
k)
Mean Amplitude (a.u)
CT D3
CT D9
col-120(sy1526) D3
l)
Mean Wavelength (a.u)
CT D3
CT D9
col-120(sy1526) D3

Figure 3

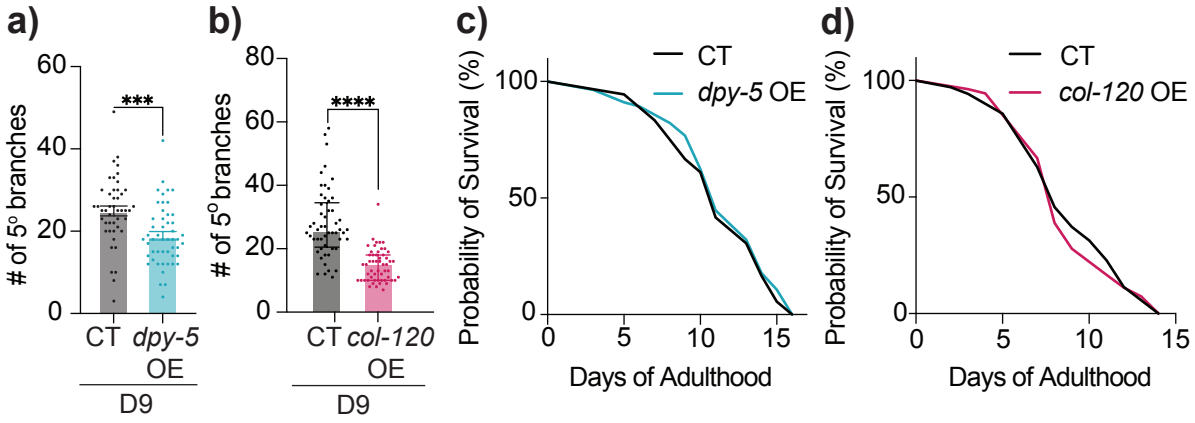
a)
b)
c)
d)
# of 5° branches
***
****
CT
dpy-5 OE
col-120 OE
D9
Probability of Survival (%)
Days of Adulthood
dpy-5 OE
col-120 OE

Figure 4

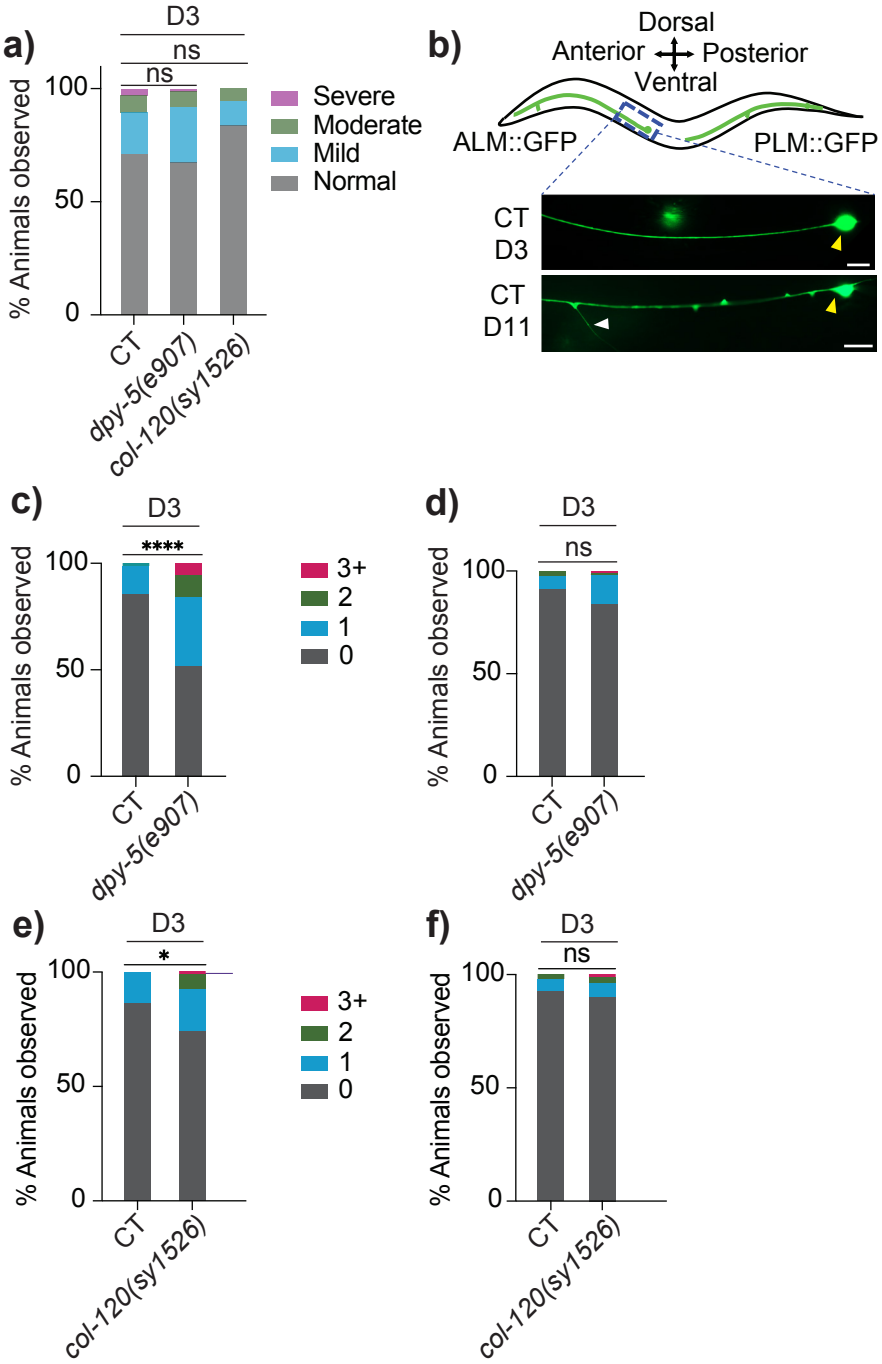
a)
D3
ns
ns
100
50
0
% Animals observed
Severe
Moderate
Mild
Normal
CT
dpy-5(e907)
col-120(sy1526)
b)
Dorsal
Anterior
Posterior
Ventral
ALM::GFP
PLM::GFP
CT
D3
CT
D11
c)
D3
****
100
50
0
% Animals observed
3+
2
1
0
CT
dpy-5(e907)
d)
D3
ns
100
50
0
% Animals observed
CT
dpy-5(e907)
e)
D3
*
100
50
0
% Animals observed
3+
2
1
0
CT
col-120(sy1526)
f)
D3
ns
100
50
0
% Animals observed
CT
col-120(sy1526)

Figure 5

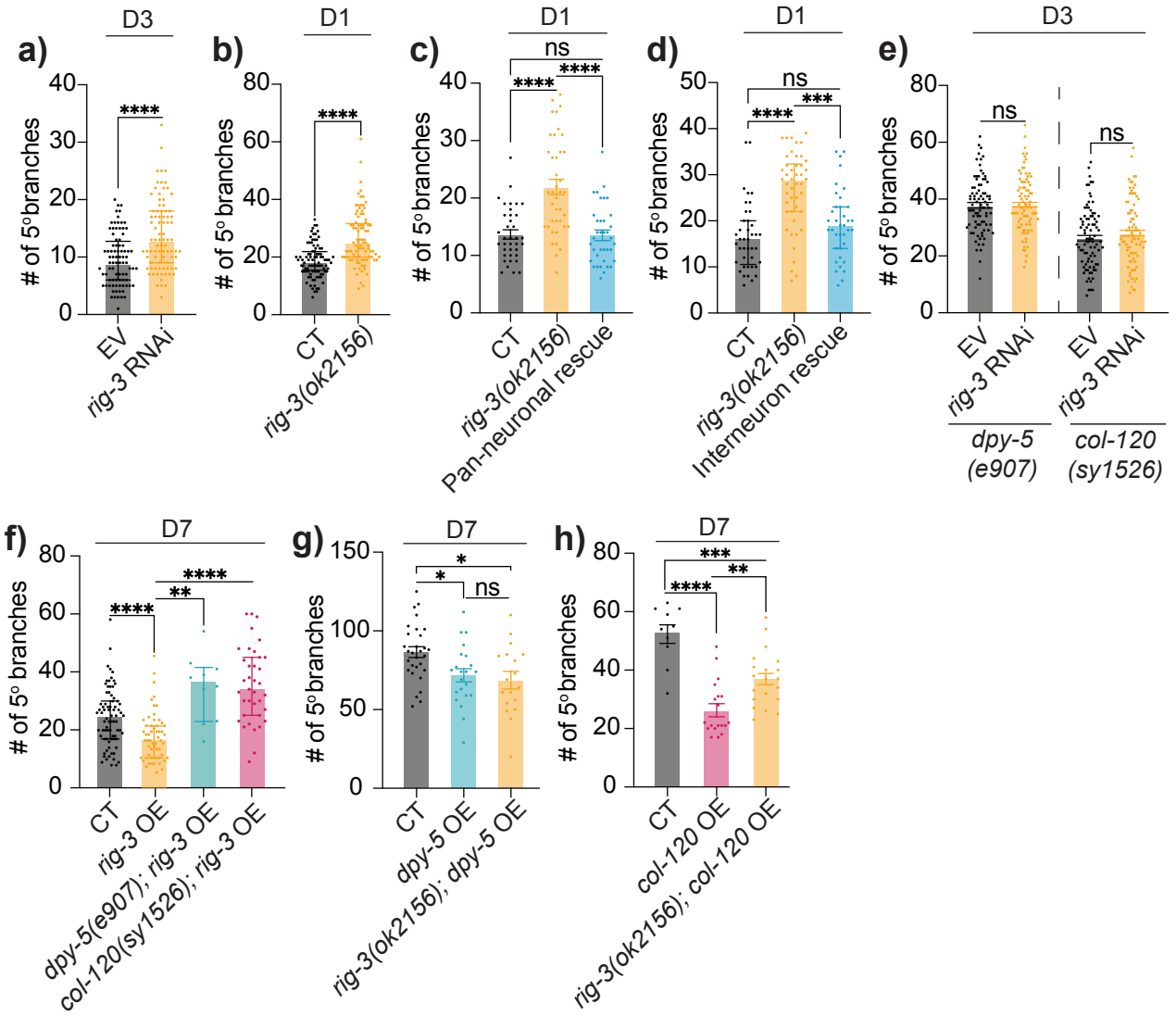
a)
D3
# of 5° branches
****
EV
rig-3 RNAi
b)
D1
# of 5° branches
****
CT
rig-3(ok2156)
c)
D1
ns
****
****
# of 5° branches
CT
rig-3(ok2156)
Pan-neuronal rescue
d)
D1
ns
****
***
# of 5° branches
CT
rig-3(ok2156)
Interneuron rescue
e)
D3
ns
ns
# of 5° branches
EV
rig-3 RNAi
EV
rig-3 RNAi
dpy-5
(e907)
col-120
(sy1526)
f)
D7
****
**
****
# of 5° branches
CT
rig-3 OE
dpy-5(e907); rig-3 OE
col-120(sy1526); rig-3 OE
g)
D7
*
*
ns
# of 5° branches
CT
dpy-5 OE
rig-3(ok2156); dpy-5 OE
h)
D7
***
**
****
# of 5° branches
CT
col-120 OE
rig-3(ok2156); col-120 OE

Figure 6

Supplemental Materials

Epidermal Collagen Reduction Drives Selective Aspects of Aging in Sensory Neurons

Meera M. Krishna[1,2], Swapnil G. Waghmare[1,2], Ariel L. Franitza[2], Emily C. Maccoux[2], Lezi E[1,2,*]

[1]Department of Cell Biology, Neurobiology and Anatomy, Medical College of Wisconsin, 8701 W Watertown Plank Road, Milwaukee, WI 53226, United States of America

[2]Neuroscience Research Center, Medical College of Wisconsin, 8701 W Watertown Plank Road, Milwaukee, WI 53226, United States of America

[*]Corresponding author/Lead contact:
lezie@mcw.edu
+1-414-955-2248

Running Title: Epidermal Collagen Reduction Drives Neuronal Aging

SUPPLEMENTAL FIGURE LEGENDS

Figure S1: Characterization of the aging PVD neuron

(a) Schematic diagram of the PVD neuron in control (CT) animals. The black box indicates the zone presented in the representative image of CT animals at Day 11 (D11) of adulthood. Yellow arrowheads indicate neuritic beads. Scale bar = 50 μM.

(b) Correlation between PVD beading severity and harsh touch response in CT [*mec-4(u253)*; *F49H12.4::GFP(wdIs51)*] animals at D7. See Methods for scoring criteria. *n* = 18.

(c-f) Number of dorsal *(c)* and ventral *(d)* 5º dendrites, and dorsal *(e)* and ventral *(f)* 6º dendrites in CT [*F49H12.4::GFP(wdIs51)*] animals at D3 (Dorsal: n = 50, Ventral: n = 55), D6 (Dorsal: n = 44, Ventral: n = 54), and D9 (Dorsal: n = 47, Ventral: n = 53).

(g) 6º dendrites in CT and *daf-16(mu86)* mutant animals at D3 and D7 (CT D3: n = 51, CT D7: n = 70, *daf-16* mutant D3: n = 47, *daf-16* mutant D7: n = 46). Experiments performed without FUDR.

(h-i) 5º *(h)* and 6º *(i)* dendrites in CT (n = 13) and *mev-1(kn1)* (n = 10). Experiments performed without FUDR.

(j) 5º dendrites in CT (n = 49) and *daf-2(e1370)* (n = 51).

(k-l) 5º *(k)* and 6º *(l)* dendrites normalized to body length in CT (n = 11) and *dpy-5(e907)* (n = 10).

(m-n) 5º *(m)* and 6º *(n)* dendrites normalized to body length in CT (D3: n = 28, D9: n = 51) and *col-120(sy1526)* (n = 25).

ns- not significant, * $p<0.05$, ** $p<0.005$, *** $p<0.001$, **** $p<0.0001$.

Figure S2: Cytoskeletal composition in PVD dendrites

(a) Split channel and merged images of microtubule localization in the PVD neuron at D7 in control (CT) animals [*ser-2(3)p::EMTB::GFP* + *ser-2(3)p::mCherry-PH(lxyEx48)*]. Red channel displays the PVD neuron, while the green channel displays the microtubules in the PVD.

(b) Split channel representative time-lapse images of actin dynamics in higher order dendrites during an 8-minute session at 2-minute intervals at D1 and D9 of adulthood in CT animals [*ser-2(3)p::GFP::UtrCH* + *ser-2(3)p::mCherry-PH(lxyEx51)*]. Red channel displays the PVD neuron, while the green channel displays the actin in the PVD.

Figure S3: Aging-associated dendritic branching correlated with proprioceptive deficits and neuritic beading

(a) Correlation between number of higher-order dendrites (5° and 6°) and harsh touch response in *mec-4(u253)* mutant animals at D7. Harsh touch response was scored based on the distance moved with a cumulative score ranging from 0 to 10, indicating impaired to normal response respectively. n = 18.

(b-c) Correlation between higher-order branching and the extent of neuritic beading in CT animals at D8 (n = 11) and D9 (n = 11). Higher-order dendrites are 5° dendrites *(b)* and 6° dendrites *(c)*. Beading severity is measured as 0- normal ,1- mild, 2- moderate, and 3- severe.

Figure S4: Characterization of cuticular collagens in aging

(a) (Left) Volcano plot depicting changes in expression of skin collagens in D10 animals relative to L4 animals from the GSE176088 dataset. *col-120, col-129, col-141, dpy-5, dpy-10, and rol-6* are shown in orange. (Right) qPCR verification of *dpy-5* and *col-120* mRNA expression levels in CT animals at D1 and D7, represented as relative quantity, with *ama-1* or *cdc-42* as housekeeping genes.

(b-c) Quantification of 5º *(b)* and 6º *(c)* dendrites in empty vector (EV) (n = 16) and *rol-6* RNAi (n = 6).

(d-e) 5º *(d)* and 6º *(e)* dendrites in EV (n = 19) and *col-129* RNAi (n = 20).

(f-g) 5º *(f)* and 6º *(g)* dendrites in CT and *col-141(gk5185)* mutant (n = 10).

(h-i) 5º *(h)* and 6º *(i)* dendrites in CT and *dpy-10(e128)* mutant (*n* = 50).

(j) mRNA levels of *dpy-5* and *col-10* (predicted paralog of *dpy-5*) after *dpy-5* RNAi clone 1 treatment *(left),* and mRNA levels of *col-120* and *dpy-3* (predicted paralog of *col-120*) after *col-120* RNAi clone 1 treatment *(right)*, relative to empty vector (EV), with *ama-1* or *cdc-42* as housekeeping genes.

(k) Comparison of body lengths between control (CT, n = 13) and *dpy-5(e907)* (n = 9).

(l) Comparison of body lengths between control (CT, n = 28) and *col-120(sy1526)* (n = 25).

(m) Summary data of lifespan analysis of CT, *dpy-5* mutant and *col-120* mutant animals.

ns- not significant, * $p<0.05$, ** $p<0.005$, *** $p<0.001$, **** $p<0.0001$.

Figure S5: Characterization of loss of *dpy-5* and *col-120*

(a) Quantification of 6° dendrites in CT(n = 50), *dpy-5(e907)* mutant (n = 50), and endogenous promoter-driven rescue (n = 49).

(b) 6° dendrites in CT, *dpy-5* mutant, and epidermis-specific rescue driven by *dpy-7p* (n = 60; line 1).

(c) 6° dendrites in CT (n = 40), *col-120(sy1526)* (n = 38), and endogenous promoter-driven rescue (n = 38).

(d) 6° dendrites in CT (n = 82), *col-120* mutant (n = 100), and epidermis-specific rescue driven by driven by *dpy-7p* and *col-19p* (n = 55; line 1).

(e-f) 5° *(e)* and 6° *(f)* dendrites in CT, *dpy-5* mutant, and epidermis-specific rescue driven by *dpy-7p* (*n* = 20; line 2).

(g-h) 5° *(g)* and 6° *(h)* dendrites in CT, *col-120* mutant, and epidermis-specific rescue driven by driven by *dpy-7p* and *col-19p* (n = 81; line 2).

(i-j) 5° *(I)* and 6° *(j)* dendrites in CT, *dpy-5* mutant, and *col-120* mutant (n = 20 for all groups).

(k-l) 5° *(k)* and 6° *(l)* dendrites in empty vector (EV) treated animals (n = 30 for both groups)**.**

(m) 5° dendrites in EV and *dpy-5* RNAi clone 1 treated animals (n = 88 for both groups).

(n) 5° dendrites in EV and *col-120* RNAi clone 1 treated animals (n = 70 for both groups)**.**

(o) Representative images of adulthood EV-treated, adulthood *dpy-5* clone 1 RNAi-treated, lifelong *dpy-5* clone 1 RNAi-treated, and *dpy-5* mutant animals at D3. Scale bar = 500 μM.

(p-q) 5° *(p)* and 6° *(q)* dendrites in EV and *dpy-5* RNAi clone 2 animals (n = 70 for both groups).

(r-s) 5° *(r)* and 6° *(s)* dendrites in EV and *col-120* RNAi clone 2 animals (n = 30 for both groups).

(t-u) Amplitude CV *(t)* and wavelength CV *(u)* in CT D3 (n = 28), CT D9 (n = 51), and *col-120* mutant (n = 25) at D3.

ns- not significant* $p<0.05$, ** $p<0.005$, *** $p<0.001$, **** $p<0.0001$.

Figure S6: Overexpression of epidermal collagens

(a) Quantification of 6º dendrites in control (CT, n = 46) and *dpy-5* epidermis-specific overexpression driven by *col-19p* (n = 50).

(b) 6º dendrites in CT (n = 53) and *col-120* epidermis-specific overexpression driven by *col-19p* (n =54; line 2).

(c-d) 5º *(c)* and 6º *(d)* dendrites in CT (n = 20) and *col-120* epidermis-specific overexpression driven by *col-19p* (n = 18; line 1).

(e) Summary of lifespan analysis of CT, *dpy-5* epidermis-specific overexpression, and *col-120* epidermis-specific overexpression line 1 animals without FUDR. Replicates in main figure indicated in bold. Same transgenic strains as in *(a)* and *(c-d)*.

(f-i) Mean amplitude *(f)*, and wavelength *(g)* normalized to control, amplitude CV *(h)*, and wavelength CV *(i)* in CT (n = 23) in *dpy-5* overexpression (same transgenic strain as in *(a)*)(n = 21).

ns- not significant, * $p<0.05$, *** $p<0.001$, **** $p<0.0001$.

Figure S7: Interactions between *rig-3*/IgSF, collagen genes, and *daf-16*/FOXO

(a-b) Quantification of 5º *(a)* and 6º *(b)* dendrites in empty vector (EV, n = 208), *ina-1* RNAi (n = 80), *ddr-2* RNAi (n = 30), *sdn-1* RNAi (n = 30), *pat-2* RNAi treatment (n = 92).

(c) 6º dendrites in EV and *rig-3* RNAi treated CT animals (*F49H12.4::GFP(wdIs51)*) *(n* = 84).

(d) 6º dendrites in CT (*ser-2(3)p::GFP(lxyEx77)*) (n = 91) and *rig-3(ok2156)* mutant (n = 90).

(e-f) 5º *(e)* and 6º *(f)* dendrites in CT and *rig-3* mutant (n = 10).

(g) 6º dendrites in CT (n = 37), *rig-3* mutant (n = 40), and pan-neuronal rescue (n = 37) (driven by *unc-33p*).

(h) 6º dendrites in CT (n = 41), *rig-3* mutant (n = 46), and interneuron rescue (n = 37) (driven by *nmr-1p*).

(i) Expression levels of *rig-3* and *nmr-1* in neuronal tissues of wild-type animals (Wormbase).

(j) 6º dendrites in *dpy-5(e907)* mutant animals treated with EV (n = 84) or *rig-3* RNAi (n = 85), as well as in *col-120(sy1526)* mutant animals treated with EV (n = 88) or *rig-3* RNAi (n = 86).

(k) 6º dendrites in CT (n = 76), *rig-3* pan-neuronal overexpression driven by *unc-33p* (n = 57), *rig-3* overexpression in *dpy-5* mutant (n = 10), and *rig-3* overexpression in *col-120* mutant (n = 37).

(l) 6º dendrites in CT (n = 30), *dpy-5* epidermis-specific overexpression driven by *col-19p* (n = 22), and *dpy-5* overexpression in *rig-3* mutant (n = 18).

(m) 6º dendrites in CT (n = 10), *col-120* epidermis-specific overexpression driven by *col-19p* (n = 19; line 1), and *col-120* overexpression in *rig-3* mutant (n = 20).

(n) KEGG pathway analysis between control and *dpy-10* mutant animals (GSE19310).

(o-p) 5º *(o)* and 6º *(p)* dendrites in CT (n = 12), *col-120* epidermis-specific overexpression driven by *col-19p* (n = 13; line 1), and *col-120* overexpression line 1 in *daf-16(mu86)* mutant background (n = 13). Experiment performed without FUDR.

ns-not significant, * $p<0.05$, ** $p<0.01$, *** $p<0.001$, **** $p<0.0001$.

Table S1: Comparison of branching in PVDL and PVDR, and Dorsal, Ventral, Anterior, and Posterior sections of PVD neuron

Difference between medians for CT animals at D3 and D9 with FUDR, and D3 and D7 without FUDR. ns-not significant, * $p<0.05$, ** $p<0.01$, *** $p<0.001$, **** $p<0.0001$.

Table S2: Correlation between excessive PVD dendritic branching and proprioceptive deficits

D3 and D9 CT animals were assayed and combined for analysis when FUDR was used for age synchronization; Data from D3 and D7 CT animals were collected when assays were conducted without FUDR. ns-not significant,* $p<0.05$, ** $p<0.01$, *** $p<0.001$, **** $p<0.0001$.

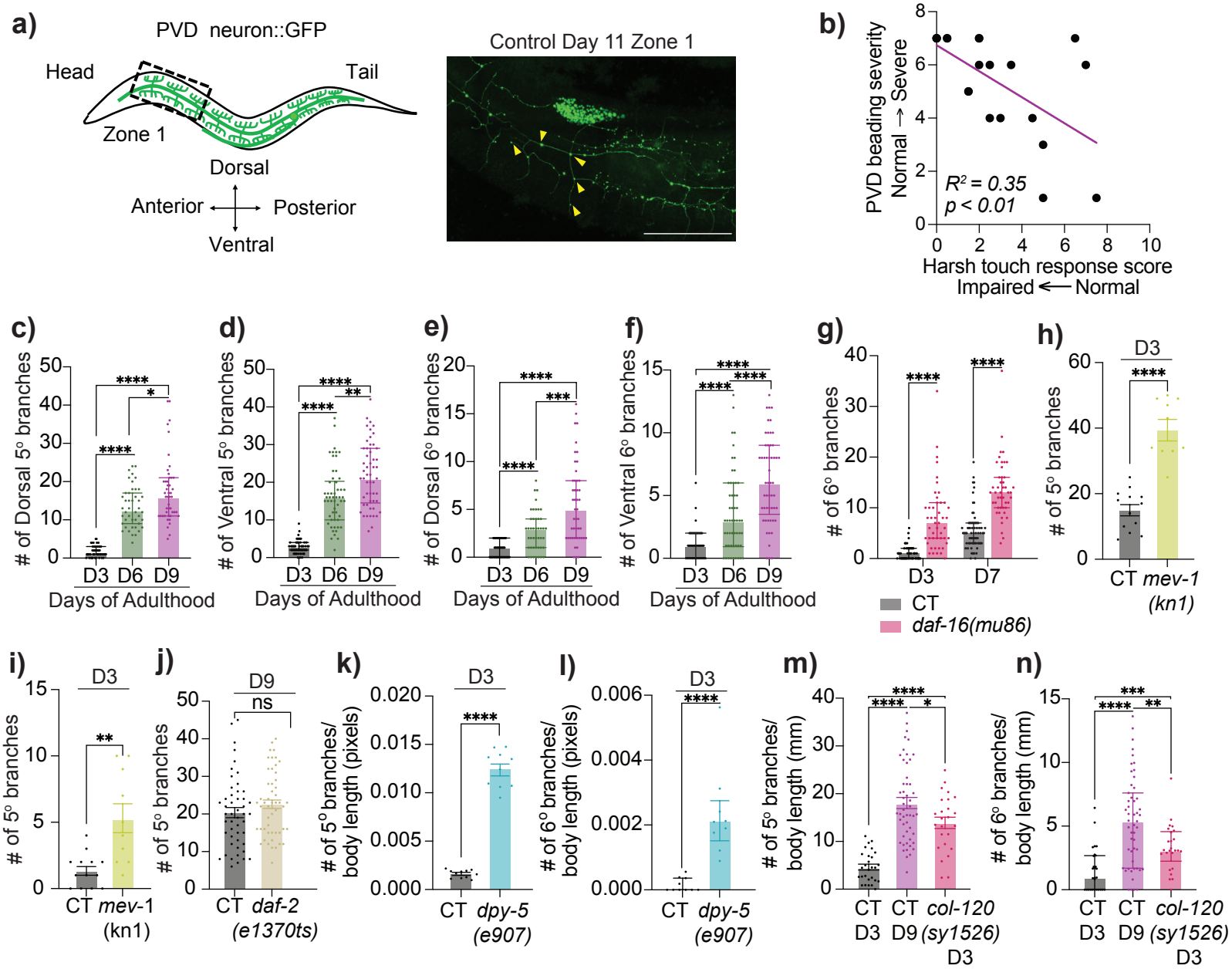

Supplemental Figure 1

a)

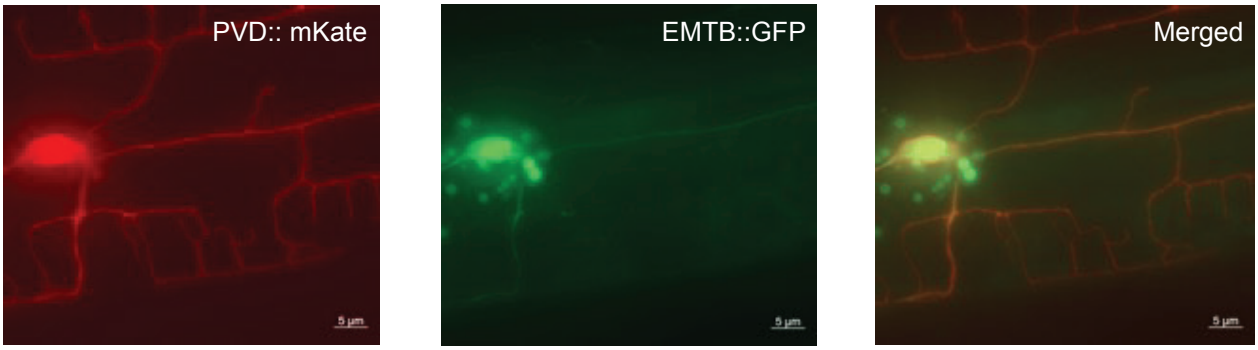

b)

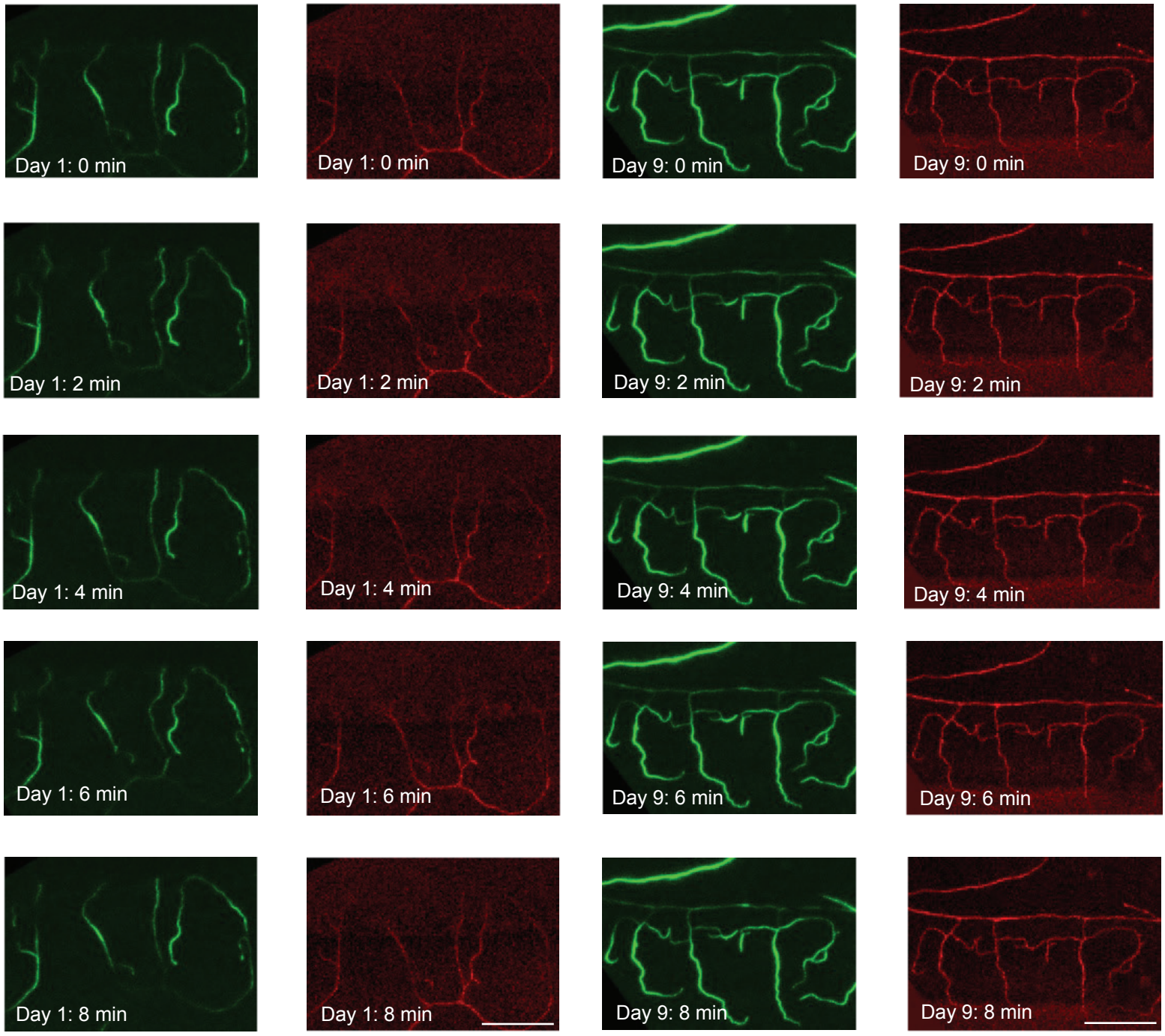

Supplemental Figure 2

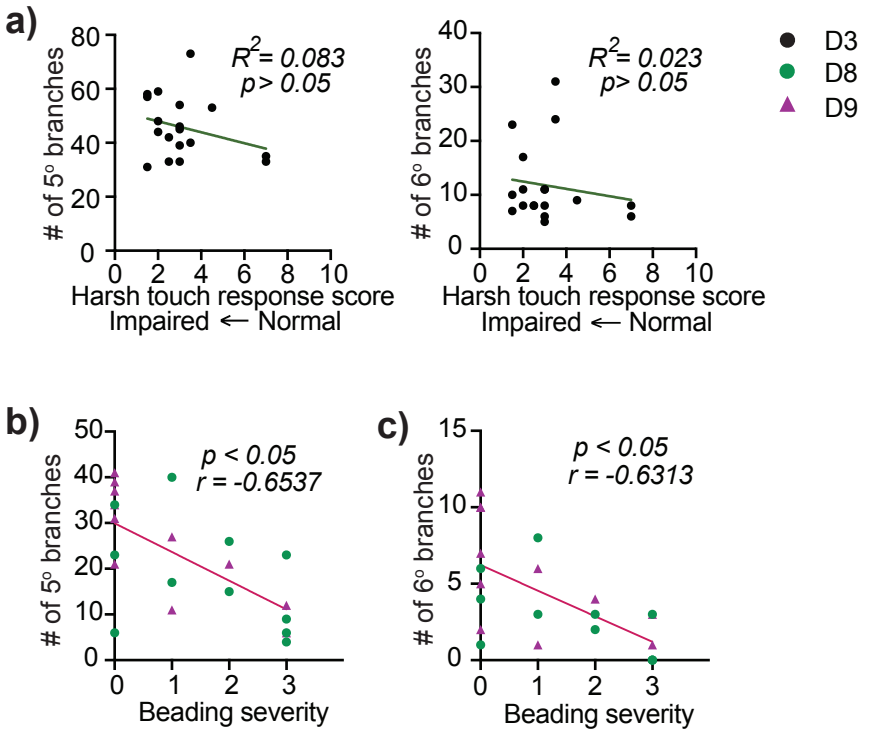

Supplemental Figure 3

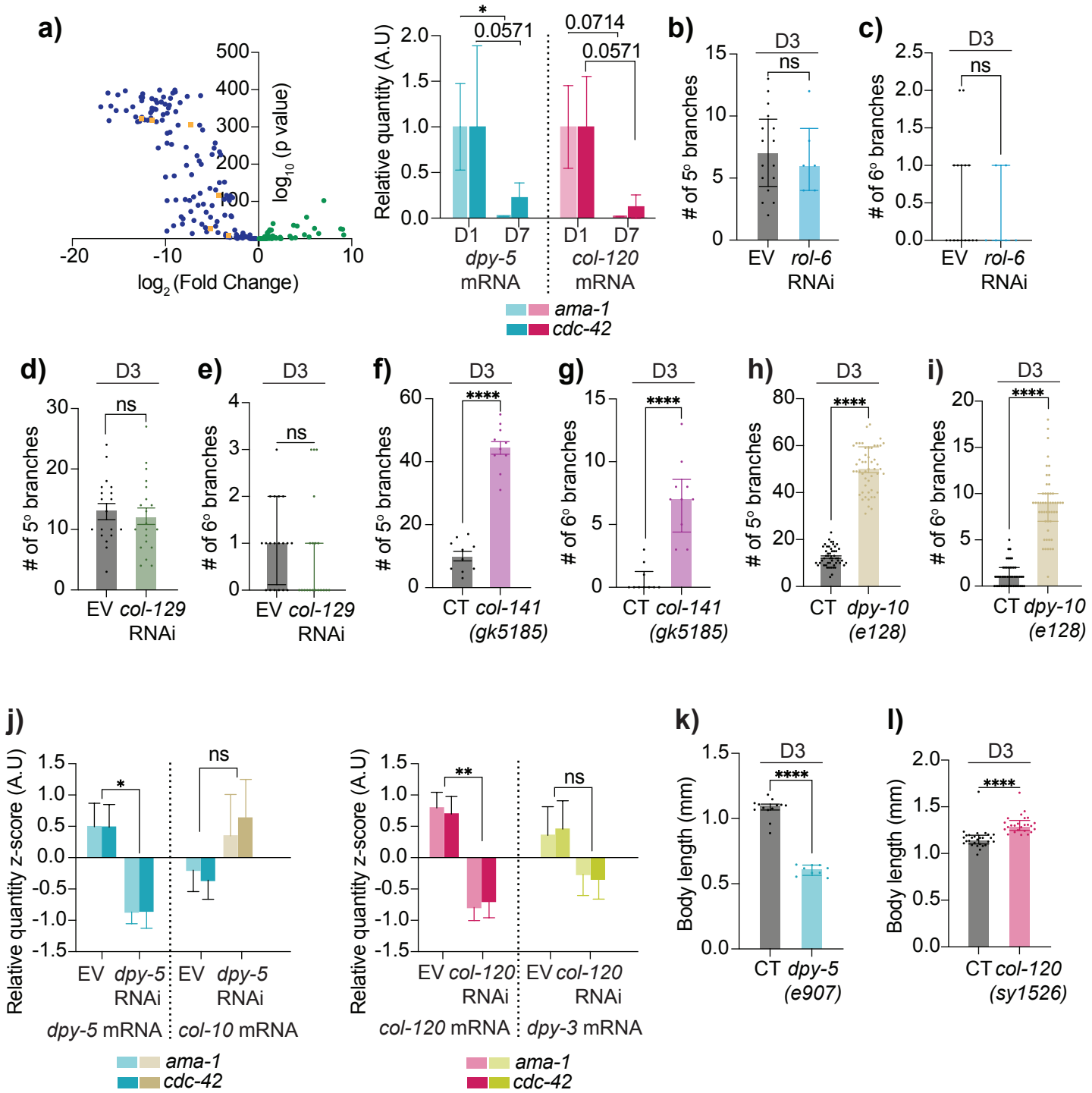

m)

Comparison	Median Lifespan	Maxiumum Lifespan	Significance vs CT (dpy-5 vs col-120)	Starting n
CT vs dpy-5 mutant vs col-120 mut rep 1	**18 vs 15.5 vs 14**	**29 vs 16 vs 18**	**0.0883 vs ***	**30; 30; 30**
CT vs *dpy-5* mutant vs *col-120* mut rep 2	22 vs 18 vs 15	25 vs 15 vs 22	* vs ****	30; 30; 30
CT vs *dpy-5* mutant vs *col-120* mut rep 3	20 vs 11.5 vs 14	25 vs 16 vs 23	*** vs **	30; 30; 30

Supplemental Figure 4

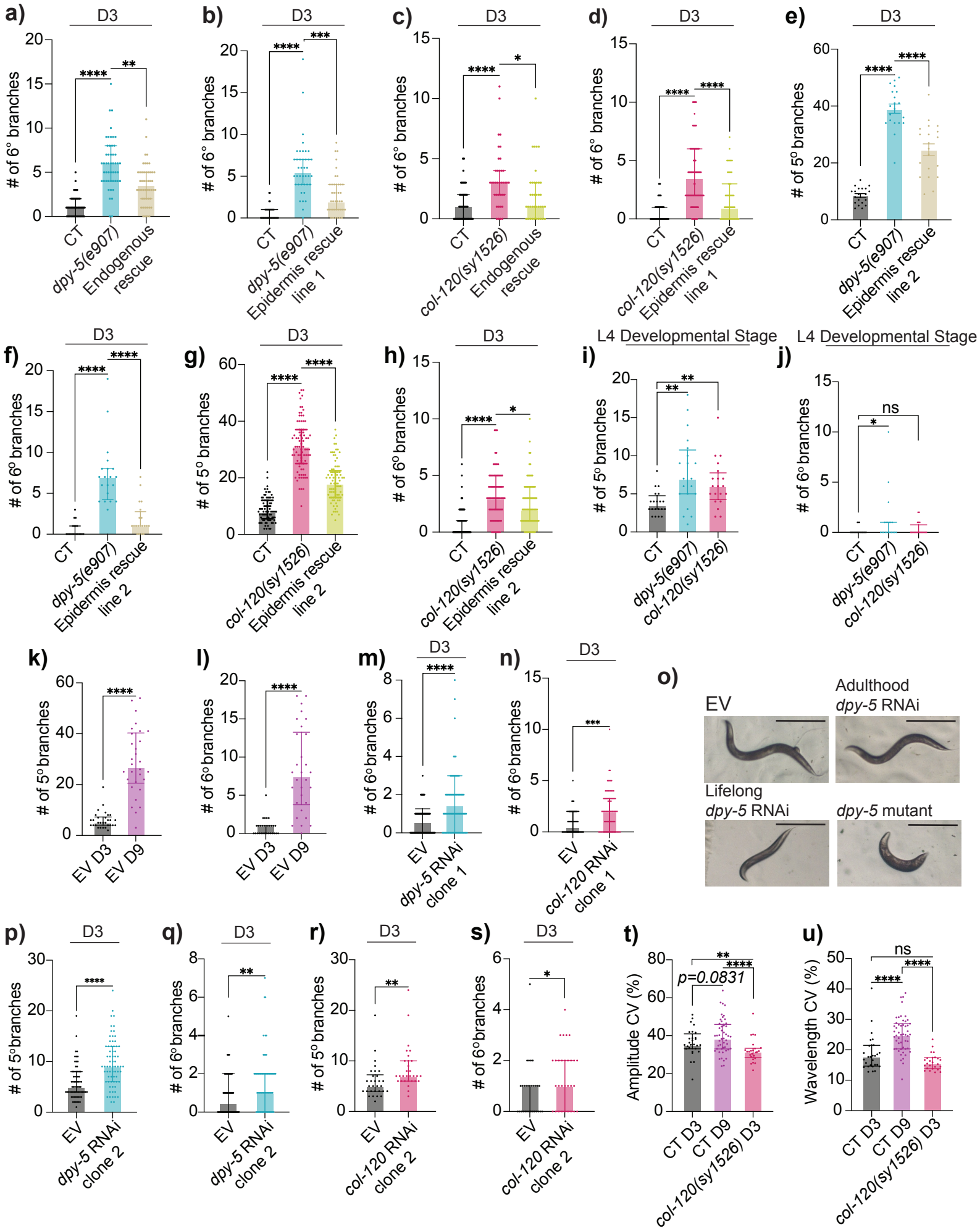

Supplemental Figure 5

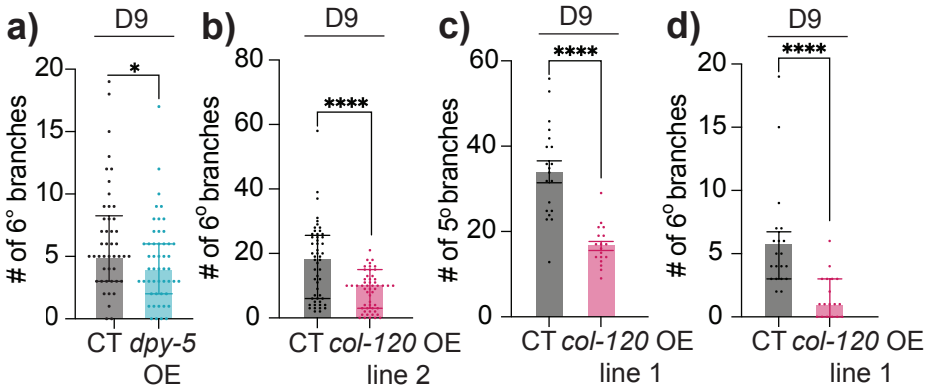

e)

Comparison	Median Lifespan	Maximum Lifespan	Significance	Starting n
CT vs dpy-5 OE rep 1	11; 11	20; 18	ns	63; 63
CT vs dpy-5 OE rep 2	**11; 11**	**16; 16**	ns	**100; 100**
CT vs dpy-5 OE rep 3	12; 10	15; 15	ns	100; 100
CT vs col-120 OE rep 1	11; 9	18; 16	*	72; 72
CT vs col-120 OE rep 2	9; 8	15; 15	ns	100; 100
CT vs col-120 OE rep 3	**8; 8**	**14; 14**	ns	**100; 100**

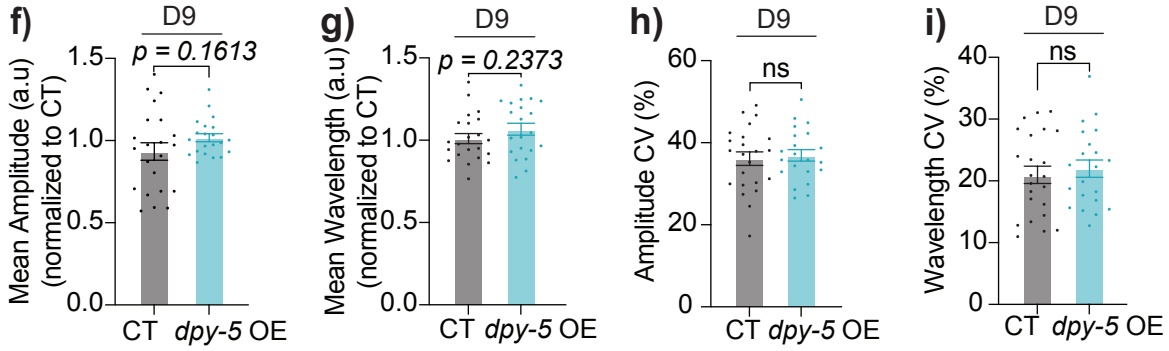

Supplemental Figure 6

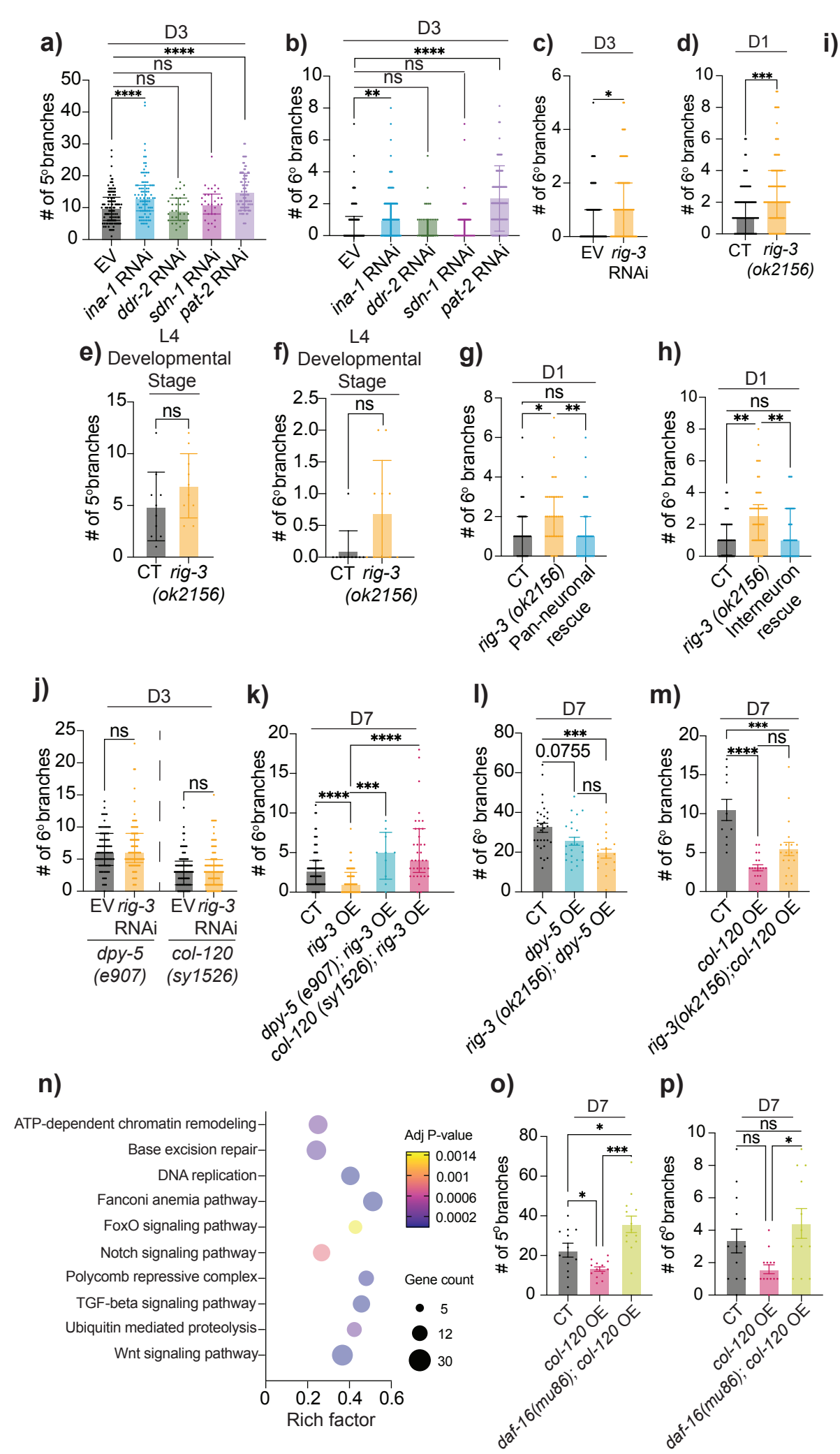

i)

rig-3 expression

Cell type	Cells (%) Expressing	Transcripts Per Million (TPM)
I4	53.03468	1052.135
I3	50	1067.467
NSM	43.00699	630.9949
PDB	40.67797	309.6697
DB	38.72153	420.6172
I1	37.37374	932.6668
AVA	35.364042	529.0081
RIH	35.2459	474.0346
MI	31.0536	396.0204
DA	29.56044	348.7844
VB01	29.26739	237.1305
AVD	28.057554	482.8923
M3	26.92308	601.7634
M4	25	335.4531
ASER	23.268698	356.8324
AVE	20.713578	332.7621
HSN	20.43011	235.2533
DB01	19.46903	144.9106
M1	18.39623	117.862
AVM	17.30769	84.1889
SMB	15.99424	112.7572
I5	14.61988	91.1973
AVB	13.744076	138.4513
AQR	13.533835	205.7389
M5	13.4715	179.0879
AVH	13.01587	111.586
RIR	12.88344	297.6041
SMD	12.72628	134.7581
RMD_DV	12.60097	203.7688
VA	11.13831	124.6461
VD_DD	10.62295	211.2284
SIB	9.816754	115.6844
PVC	9.448819	82.1599
RIA	9.393451	113.7795
AS	9.0771558	159.8174
URB	8.571429	52.8631
I6	8.064516	351.5068
AWC_ON	7.924528	80.3531
AVF	7.913669	71.6413
ASEL	7.1794872	80.7719
RID	7.148888	31.3134
VB	7.075472	70.1037
VB02	6.998088	54.4419
AIZ	6.867356	47.4251
PLN	6.688963	66.0832
DVA	6.557377	81.8664
RMD_LR	6.372549	85.9478
M2	6.113033	86.5894
AWC_OFF	5.857741	70.2421
ALA	5.462185	22.761
IL2_DV	5	39.6587
AIB	4.922516	27.7879
VA12	4.878049	83.8366
MC	4.849885	154.2685
RIB	4.48	78.3109
SAB	4.081633	91.8373
SAA	4.040404	72.0016
AVJ	3.926941	48.8293
IL2_LR	3.529412	18.8917
OLQ	3.529412	57.6456
IL1	3.448276	128.3607
ASH	2.675585	41.7272
BDU	2.650602	18.0707
AFD	2.448979	28.9723
RIP	2.380952	30.7552
RMF	2.290076	20.8604
PVT	2.272727	12.8807

nmr-1 expression

Cell type	Cells (%) Expressing	Transcripts Per Million (TPM)
PVC	23.62205	378.31377
AVD	21.582734	401.18426
AVA	15.89896	202.41909
AVE	14.370664	224.85122
AVG	12.41535	131.0069
RIM	9.52381	89.8226
AVF	3.23741	60.86642
SIB	2.356021	27.08129
RIP	1.190476	14.24181

Table S1

Comparison	with FUDR			no FUDR		
	CT D3	CT D9	Significance	CT D3	CT D7	Significance
Number of Right 5º branches	2.0 (n = 58)	20.0 (n = 58)	****	13.0 (n = 44)	28.0 (n = 29)	****
Number of Left 5º branches	2.0 (n = 47)	16.0 (n = 42)	****	10.50 (n =50)	27.00 (n = 41)	****
Number of Right 6º branches	1.0 (n = 58)	5.5 (n = 58)	****	1.0 (n = 44)	5.0 (n = 29)	****
Number of Left 6º branches	1.0 (n = 47)	5.5 (n = 42)	****	1.0 (n = 50)	5.0 (n = 41)	****
Number of Dorsal menorahs	16.5 (n = 10)	20.0 (n = 11)	ns	19.0 (n = 21)	16.0 (n = 19)	**
Number of Ventral menorahs	17.0 (n = 20)	16.0 (n = 14)	ns	16.5 (n = 22)	16.0 (n = 39)	ns
Number of Anterior menorahs	12.5 (n = 30)	13.0 (n = 25)	ns	13.0 (n = 43)	11.0 (n = 58)	***
Number of Posterior menorahs	5.0 (n = 30)	5.0 (n = 25)	ns	5.0 (n = 43)	5.0 (n = 58)	ns
Number of Dorsal 4º branches	66.0 (n = 10)	78.0 (n = 11)	ns	67.0 (n = 21)	68.0 (n = 19)	ns
Number of Ventral 4º branches	66.0 (n = 20)	72.5 (n = 14)	ns	77.0 (n = 22)	75.0 (n = 39)	ns
Number of Anterior 4º branches	40.0 (n = 30)	44.0 (n = 25)	*	47.0 (n = 43)	45.0 (n = 58)	ns
Number of Posterior 4º branches	26.0 (n = 30)	29.0 (n = 25)	ns	25.0 (n = 43)	25.0 (n = 58)	ns
Number of Dorsal 5º branches/ Dorsal menorah	0.5045 (n = 10)	2.000 (n = 11)	***	0.0625 (n = 21)	0.3158 (n = 19)	****
Number of Ventral 5º branches/ Ventral menorah	0.1563 (n = 20)	0.3643 (n = 14)	****	0.0816 (n = 22)	0.3571 (n = 39)	****
Number of Anterior 5º branches/ Anterior menorah	0.2020 (n = 30)	1.1670 (n = 25)	****	0.0000 (n = 43)	0.2000 (n = 58)	****
Number of Posterior 5º branches/ Posterior menorah	1.3750 (n = 30)	3.0000 (n = 25)	****	0.1667 (n = 43)	0.6333 (n = 58)	****
Number of Dorsal 5º branches/ Dorsal 4º branches	0.1257 (n = 10)	0.4103 (n = 11)	***	0.0161 (n = 21)	0.0641 (n = 19)	***
Number of Ventral 5º branches/ Ventral 4º branches	0.1563 (n = 20)	0.3643 (n = 14)	****	0.0160 (n = 22)	0.0806 (n = 39)	****
Number of Anterior 5º branches/ Anterior 4º branches	0.0519 (n = 30)	0.3056 (n = 25)	****	0.0000 (n = 43)	0.0454 (n = 58)	****
Number of Posterior 5º branches/ Posterior 4º branches	1.3750 (n = 30)	3.0000 (n = 25)	****	0.0357 (n = 43)	0.1200 (n = 58)	****
Number of Dorsal 6º branches/ Dorsal menorah	0.0000 (n = 10)	0.2500 (n = 11)	**	Refer to Figure 1		
Number of Ventral 6º branches/ Ventral menorah	0.0000 (n = 20)	0.1333 (n = 14)	***			
Number of Anterior 6º branches/ Anterior menorah	0.0000 (n = 30)	0.0909 (n = 25)	****			
Number of Posterior 6º branches/ Posterior menorah	0.0000 (n = 30)	0.4000 (n = 25)	****			
Number of Dorsal 6º branches/ Dorsal 4º branches	0.0000 (n = 10)	0.0635 (n = 11)	**			
Number of Ventral 6º branches/ Ventral 4º branches	0.0000 (n = 20)	0.0329 (n = 14)	**			
Number of Anterior 6º branches/ Anterior 4º branches	0.0000 (n = 30)	0.0238 (n = 25)	****			
Number of Posterior 6º branches/ Posterior 4º branches	0.0000 (n = 30)	0.0689 (n = 25)	****			

Table S2

Correlation	with FUDR			no FUDR		
	p value	*r* value	*n*	*p* value	*r* value	*n*
Dorsal 5º branches – Mean Wavelength	0.0613	-0.2666	49	***	-0.5883	34
Ventral 5º branches – Mean Wavelength	ns	-0.0218	30	ns	-0.1296	44
Dorsal 5º branches – Mean Amplitude	ns	-0.2369	49	***	-0.5878	34
Ventral 5º branches – Mean Amplitude	ns	0.0913	30	ns	-0.2042	44
Dorsal 5º branches – Wavelength CV	**	0.3706	49	****	0.6785	34
Ventral 5º branches – Wavelength CV	ns	0.2933	30	*	0.3375	44
Dorsal 5º branches – Amplitude CV	0.0829	0.2505	49	***	0.5494	34
Ventral 5º branches – Amplitude CV	ns	-0.0141	30	**	0.3947	44
Dorsal 6º branches – Mean Wavelength	0.0747	-0.2570	49	*	-0.3517	34
Ventral 5º branches – Mean Wavelength	ns	0.0631	30	ns	0.2477	44
Dorsal 6º branches – Mean Amplitude	**	-0.3656	49	0.0721	-0.3123	34
Ventral 6º branches – Mean Amplitude	ns	0.2818	30	0.0622	-0.2835	44
Dorsal 6º branches – Wavelength CV	**	0.5012	49	*	0.3714	34
Ventral 6º branches – Wavelength CV	ns	0.1033	30	***	0.5239	44
Dorsal 6º branches – Amplitude CV	****	0.5731	49	**	0.4680	34
Ventral 6º branches – Amplitude CV	ns	-0.0747	30	**	0.4649	44
5º branches – Mean Wavelength	ns	-0.1710	79	Refer to Figure 2		
5º branches – Mean Amplitude	ns	-0.1222	79			
5º branches – Wavelength CV	**	0.3380	79			
5º branches – Amplitude CV	ns	0.1540	79			
6º branches – Mean Wavelength	0.0623	-0.2107	79	*	-0.2888	78
6º branches – Mean Amplitude	ns	-0.1338	79	**	-0.3031	78
6º branches – Wavelength CV	**	0.3402	79	****	0.4720	78
6º branches – Amplitude CV	**	0.3343	79	****	0.4731	78